



Seventeen Tidal Disruption Events from the First Half of ZTF Survey Observations: Entering a New Era of Population Studies

Sjoert van Velzen^{1,2}, Suvi Gezari^{1,3}, Erica Hammerstein¹, Nathaniel Roth^{1,3}, Sara Frederick¹, Charlotte Ward¹,
Tiara Hung⁴, S. Bradley Cenko^{3,5}, Robert Stein⁶, Daniel A. Perley⁷, Kirsty Taggart⁷, Ryan J. Foley⁴, Jesper Sollerman⁸,
Nadejda Blagorodnova⁹, Igor Andreoni¹⁰, Eric C. Bellm¹¹, Valery Brinnel¹², Kishalay De¹⁰, Richard Dekany¹³,
Michael Feeney¹³, Christoffer Fremling¹⁰, Matteo Gioni¹⁴, V. Zach Golkhou^{11,15}, Matthew J. Graham¹⁰,
Anna. Y. Q. Ho¹⁰, Mansi M. Kasliwal¹⁰, Charles D. Kilpatrick⁴, Shrinivas R. Kulkarni¹⁰, Thomas Kupfer¹⁵,
Russ R. Laher¹⁶, Ashish Mahabal^{10,17}, Frank J. Masci¹⁶, Adam A. Miller^{18,19}, Jakob Nordin¹², Reed Riddle¹³,
Ben Rusholme¹⁶, Jakob van Santen⁶, Yashvi Sharma¹⁰, David L. Shupe¹⁶, and Maayane T. Soumagnac^{20,21}

¹ Department of Astronomy, University of Maryland, College Park, MD 20742, USA; sjoert@nyu.edu

² Center for Cosmology and Particle Physics, New York University, NY 10003, USA

³ Joint Space-Science Institute, University of Maryland, College Park, MD 20742, USA

⁴ Department of Astronomy and Astrophysics, University of California, Santa Cruz, CA 95064, USA

⁵ Astrophysics Science Division, NASA Goddard Space Flight Center, MC 661, Greenbelt, MD 20771, USA

⁶ Deutsches Elektronensynchrotron, Platanenallee 6, D-15738, Zeuthen, Germany

⁷ Astrophysics Research Institute, Liverpool John Moores University, 146 Brownlow Hill, Liverpool L3 5RF, UK

⁸ The Oskar Klein Centre & Department of Astronomy, Stockholm University, AlbaNova, SE-106 91 Stockholm, Sweden

⁹ Department of Astrophysics/IMAPP, Radboud University Nijmegen, P.O. Box 9010, 6500 GL Nijmegen, The Netherlands

¹⁰ Division of Physics, Mathematics, and Astronomy, California Institute of Technology, Pasadena, CA 91125, USA

¹¹ DIRAC Institute, Department of Astronomy, University of Washington, 3910 15th Avenue NE, Seattle, WA 98195, USA

¹² Institute of Physics, Humboldt-Universität zu Berlin, Newtonstr. 15, D-12489 Berlin, Germany

¹³ Caltech Optical Observatories, California Institute of Technology, Pasadena, CA 91125, USA

¹⁴ The eScience Institute, University of Washington, Seattle, WA 98195, USA

¹⁵ Kavli Institute for Theoretical Physics, University of California, Santa Barbara, CA 93106, USA

¹⁶ IPAC, California Institute of Technology, 1200 E California Boulevard, Pasadena, CA 91125, USA

¹⁷ Center for Data Driven Discovery, California Institute of Technology, Pasadena, CA 91125, USA

¹⁸ Center for Interdisciplinary Exploration and Research in Astrophysics (CIERA) and Department of Physics and Astronomy, Northwestern University, 2145 Sheridan Road, Evanston, IL 60208, USA

¹⁹ The Adler Planetarium, Chicago, IL 60605, USA

²⁰ Lawrence Berkeley National Laboratory, 1 Cyclotron Road, Berkeley, CA 94720, USA

²¹ Department of Particle Physics and Astrophysics, Weizmann Institute of Science, Rehovot 76100, Israel

Received 2020 January 13; revised 2020 October 6; accepted 2020 October 9; published 2021 February 8

Abstract

While tidal disruption events (TDEs) have long been heralded as laboratories for the study of quiescent black holes, the small number of known TDEs and uncertainties in their emission mechanism have hindered progress toward this promise. Here we present 17 new TDEs that have been detected recently by the Zwicky Transient Facility along with Swift UV and X-ray follow-up observations. Our homogeneous analysis of the optical/UV light curves, including 22 previously known TDEs from the literature, reveals a clean separation of light-curve properties with spectroscopic class. The TDEs with Bowen fluorescence features in their optical spectra have smaller blackbody radii, lower optical luminosities, and higher disruption rates compared to the rest of the sample. The small subset of TDEs that show only helium emission lines in their spectra have the longest rise times, the highest luminosities, and the lowest rates. A high detection rate of Bowen lines in TDEs with small photometric radii could be explained by the high density that is required for this fluorescence mechanism. The stellar debris can provide a source for this dense material. Diffusion of photons through this debris may explain why the rise and fade timescale of the TDEs in our sample are not correlated. We also report, for the first time, the detection of soft X-ray flares from a TDE on \sim day timescales. Based on the fact that the X-ray flares peak at a luminosity similar to the optical/UV blackbody luminosity, we attribute them to brief glimpses through a reprocessing layer that otherwise obscures the inner accretion flow.

Unified Astronomy Thesaurus concepts: [Astrophysical black holes \(98\)](#); [Tidal disruption \(1696\)](#); [Galaxy nuclei \(609\)](#)

Supporting material: data behind figure, tar.gz file

1. Introduction

The occasional ($\sim 10^{-4}$ yr $^{-1}$) luminous flare of radiation from a galaxy nucleus due to the tidal disruption of a star by an otherwise dormant central massive black hole originated as a theoretical concept (Lidskii & Ozernoi 1979; Rees 1988), but thanks to the rapid increase in wide-field survey capabilities across the electromagnetic spectrum, it is now a well-established

class of transients. While the first candidates were detected as soft X-ray outbursts in previously quiescent galaxy nuclei by the ROSAT All-Sky Survey (Donley et al. 2002), these tidal disruption events (TDEs) have more recently emerged as a unique class of nuclear transients in optical surveys with common photometric properties: persistent blue colors, a relatively long rise time compared to most supernovae (SNe),

and a smooth, power-law decline from peak (van Velzen et al. 2011, 2019e; Hung et al. 2017). The spectroscopic features of TDEs are characterized by a hot, blue thermal continuum and very broad $((5\text{--}15) \times 10^3 \text{ km s}^{-1}$; Arcavi et al. 2014; Hung et al. 2017) emission lines, which are distinct from nearly all SNe (when observed postpeak) and active galactic nuclei (AGNs). The inferred volumetric rate of photometric and spectroscopic TDEs class falls off steeply above the “Hills mass,” for which a star can be disrupted before disappearing behind the black hole event horizon (Hills 1975), further strengthening the association of this class of transients as bona fide stellar disruptions (van Velzen 2018).

However, while discoveries of TDEs are becoming increasingly more common in wide-field optical surveys such as iPTF (Blagorodnova et al. 2017, 2019; Hung et al. 2017), ZTF (van Velzen et al. 2019e), ASAS-SN (Holoien et al. 2014, 2016a, 2016b, 2019a; Wevers et al. 2019b), and Pan-STARRS (Gezari et al. 2012; Chornock et al. 2014; Holoien et al. 2019b; Nicholl et al. 2019a), the nature of what is powering their relatively uniform optical light curves is uncertain. Unlike the soft X-ray component detected in some optically selected TDEs, which is consistent with thermal emission from the inner radii of an accretion disk (Komossa 2015; Miller et al. 2015; Gezari et al. 2017; van Velzen et al. 2019e; Wevers et al. 2019b), the inferred blackbody radius of the UV/optical thermal component is a factor of 10–100 larger than expected for the size of the nascent debris disk expected to form from the circularization of the stellar debris streams. This implies the existence of an unknown, larger structure, potentially produced as a result of an outflow or wind (Miller 2015; Metzger & Stone 2017; Dai et al. 2018), or the intersecting debris streams themselves (Piran et al. 2015; Jiang et al. 2016; Bonnerot et al. 2017). Indeed, there are now several examples of outflow signatures from optical (Hung et al. 2019), UV (Cenko et al. 2016; Blagorodnova et al. 2018; Brown et al. 2018), and X-ray (Miller et al. 2015; Kara et al. 2017) spectroscopy, plus potentially also in the radio (Alexander et al. 2016, 2017)—however, see van Velzen et al. (2016), Pasham & van Velzen (2018) for a different explanation of the radio emission from optical TDEs.

There has been a recent expansion of spectroscopic subclasses for TDEs, from the first optical TDE spectra (van Velzen et al. 2011; Gezari et al. 2012), one of which surprisingly showed only broad He II lines and no hydrogen emission (Gezari et al. 2012), to the He-rich to H-rich sequence proposed by Arcavi et al. (2014), to including classes with Bowen fluorescence emission-line features (Blagorodnova et al. 2018; Leloudas et al. 2019), low-ionization Fe II lines (Wevers et al. 2019b), as well as a TDE that showed the gradual disappearance of broad H lines, while the broad He II λ 4686 line remained strong (Nicholl et al. 2019a). The UV spectra of TDEs are also unique, characterized by strong N III] λ 1750 emission but weak Mg II λ 2896, 2803 and C III] λ 1909 (Cenko et al. 2016). The nature of this spectral diversity has been attributed to the chemical composition of the star (Gezari et al. 2012; Kochanek 2016), ionization state of the debris (Guillochon et al. 2014), radiative transfer effects in an optically thick envelope (Roth et al. 2016), and reprocessing of X-ray emission through dense, optically thick gas (Leloudas et al. 2019; Wevers et al. 2019b).

In this paper, we present the largest spectroscopic TDE sample to date. We discovered correlations between the spectroscopic subclass of the TDE and the host-galaxy and flare properties. These correlation provide new insights into the origin of the spectral diversity in TDEs.

We were able to discover these correlations thanks to a homogeneous treatment of well-sampled optical/UV light curves of 31 spectroscopic TDEs. This factor of ≈ 2 increase in sample size of known TDEs can, for a large part, be attributed to the start of the Zwicky Transient Facility (ZTF; Bellm et al. 2019b) in 2018 March. We searched the ZTF data for new TDEs using a combination of photometric selection and spectroscopic and multiwavelength follow-up (van Velzen et al. 2019e). While ZTF is not always the first survey to report these events to the Transient Name Server (TNS) and thus claim discovery credit (see Table 1), for most sources, ZTF provides the deepest difference-imaging light curves that are publicly available (Masci et al. 2019; Patterson et al. 2019).

Besides the origin of optical emission, a second important (and unexpected) observation of optically selected TDEs is their X-ray faintness. The most common explanation is that the soft X-rays from accretion in the inner disk are absorbed and reprocessed into optical photons (e.g., Guillochon et al. 2014; Auchettl et al. 2017; Dai et al. 2018). In this scenario, the X-rays can only break out after the obscuring gas has expanded enough to become transparent to X-rays (Metzger & Stone 2016; Lu & Kumar 2018). However, intrinsically faint soft X-ray TDEs have also been proposed as a result of delayed accretion due to the timescale required for the circularization of the debris into an appreciable accretion disk (Piran et al. 2015; Krolik et al. 2016; Gezari et al. 2017). Discriminating between these models, and thus determining if the optical emission is powered by accretion or the stream kinetic energy, is possible by looking at the relative timing and response of the optical flare to the soft X-ray emission from TDEs (Pasham et al. 2017). Significant soft X-ray variability has recently been observed, including a late-time brightening that is anticorrelated with the smooth decline of the optical component (Gezari et al. 2017; van Velzen et al. 2019e; Wevers et al. 2019b). In this paper, we present four more optically selected TDEs with soft X-ray detections, including both flaring and late-time X-ray brightening, which provide new constraints on the emission mechanisms.

In Section 2, we present the selection of TDE candidates from the ZTF stream and spectroscopic follow-up, as well as our naming scheme for three spectroscopic classes. In Section 3, we investigate the host galaxies of our TDEs, obtaining estimates of their mass and star formation histories, followed by Section 4, which contains the details of our multiwavelength follow-up observations. In Section 5, we present our light-curve model that is applied to 39 spectroscopic+photometric TDEs. In Section 6, we present correlations between features extracted from our light-curve model, plus a discovery of differences in the photometric features between the TDEs of each spectroscopic class.

We adopt a flat cosmology with $\Omega_{\Lambda} = 0.7$ and $H_0 = 70 \text{ km s}^{-1} \text{ Mpc}^{-1}$. All magnitudes are reported in the AB system (Oke 1974).

2. Candidate Selection and Classification

2.1. Zwicky Transient Facility

Our search for new TDEs is done exclusively using ZTF data. The strength of ZTF (Graham et al. 2019) is a combination of depth (limiting magnitude of $m \approx 20.5$ per visit) and area (47 deg^2 field of view). Most of our sources originate from the public MSIP survey, which aims (Bellm et al. 2019a) to visit the entire visible northern sky every three nights in both the g and r

Table 1
Names and Discovery Name (in Boldface)

IAU Name	ZTF Name	GOT Name	Other/Discovery Name	First TDE Classification Report
AT2018zr	ZTF18aabtxvd	Ned	PS18kh	ATel#11444 (Tucker et al. 2018)
AT2018bsi	ZTF18aahqkbt	Jon		ATel#12035 (Gezari et al. 2018)
AT2018hco	ZTF18abxftqm	Sansa	ATLAS18way	ATel#12263 (van Velzen et al. 2018)
AT2018iih	ZTF18acaqdaa	Jorah	ATLAS18yzs , Gaia18dpo	This paper
AT2018hyz	ZTF18acpdvos	Gendry	ASASSN-18zj , ATLAS18bafs	ATel#12198 (Dong et al. 2018)
AT2018ini	ZTF18actaqdw	Arya		This paper
AT2018lna	ZTF19aabbnzo	Cersei		ATel#12509 (van Velzen et al. 2019d)
AT2019cho	ZTF19aakiwze	Petyr		This paper
AT2019bhf	ZTF19aakswrb	Varys		This paper
AT2019azh	ZTF17aaazdb ^a	Jaime	ASASSN-19dj , Gaia19bvo	ATel#12568 (van Velzen et al. 2019a) ^b
AT2019dsg	ZTF19aapreis	Bran	ATLAS19kl	ATel#12752 (Nicholl et al. 2019b)
AT2019ehz	ZTF19aarioci	Brienne	Gaia19bpt	ATel#12789 (Gezari et al. 2019)
AT2019eve	ZTF19aatylnl	Catelyn	Gaia19bti, ATLAS19kfv	This paper
AT2019mha	ZTF19abhejal	Bronn	ATLAS19qqu	This paper
AT2019meg	ZTF19abhhjcc	Margaery	Gaia19dhd	AN-2019-88 (van Velzen et al. 2019b) ^c
AT2019lww	ZTF19abidbya	Robb	ATLAS19rnz, PS19ega	This paper
AT2019qiz	ZTF19abzrhgq	Melisandre	ATLAS19vfr, Gaia19eks, PS19gdd	ATel#13131 (Siebert et al. 2019)

Notes. Names in boldface indicate the discovery name, i.e., the first survey to report photometry of the transient detection to the TNS.

^a The year 2017 in the ZTF name of this transient is due to a detection by the IPAC alert photometry pipeline at the end of the ZTF commission phase, although after visual inspection of the difference image, we flag this measurement as spurious.

^b First spectrum obtained by Heikkilä et al. (2019) on 2019 February 21 but classification not yet conclusive.

^c First spectrum published by Nicholl et al. (2019c) on 2019 August 1 but classification not yet conclusive.

filters. The use of two filters is an essential ingredient to our TDE selection pipeline, as it allows for efficient photometric filtering (Figure 1) to narrow down the number of targets for spectroscopic follow-up observations.

2.2. ZTF Alert Filtering

We use the information from the data stream (Patterson et al. 2019) of ZTF alerts, which is produced at IPAC and contains the difference-imaging photometry and astrometry of transients and variable sources (Maschi et al. 2019).

We place no requirement on the host-galaxy type or color. However, we reject galaxies that can be spectroscopically classified as broad-line AGNs. This rejection step implies that our sample will not contain TDE candidates in broad-line AGNs, such as PS16dtm (Blanchard et al. 2017). For AGN identification we use the Million Quasars Catalog (Flesch 2015, v5.2.). In addition, we construct a light curve from the NeoWISE (Mainzer et al. 2011) photometry and reject any galaxies with significant variability ($\chi^2/\text{dof} > 10$) or a mean $W1 - W2$ color that exceeds the AGN threshold of Stern et al. (2012). Our filter is executed by Ampel (Nordin et al. 2019), which includes fast catalog matching by catsHTM (Soumagnac & Ofek 2018), and we use the GROWTH marshal (Kasliwal et al. 2019) to coordinate our follow-up observations and spectroscopic classifications.

Compared to our TDE search in ZTF commissioning data (van Velzen et al. 2019e), we use a more liberal cut on the star-galaxy score (Tachibana & Miller 2018) of < 0.8 . This increases the galaxy sample at the cost of a much higher background due to bright variable stars (these often have a score equal to 0.5 due to issues with the PS1 photometry for bright and variable objects). We therefore veto the star-galaxy score if the source has a detected parallax in Gaia DR2 (Gaia Collaboration et al. 2016, 2018) or if the ratio of the Gaia G -band flux to the PS1 PSF g , r , i flux (converted to the G band) is consistent with a point source. Because we require a match to

a known source in the ZTF reference image, we can use a relatively liberal cut on the real-bogus score (Mahabal et al. 2019) of 0.3.

As demonstrated in Figure 1, TDEs can be discriminated from SNe and AGNs based on their rise/fade timescale, $g - r$ color, and lack of color evolution. We rank photometric TDE candidates for spectroscopic follow-up based on their distance from the locus of photometric properties of SNe. In general, we rejected transients that are significantly off-center (mean offset $> 0''.4$), or have significant $g - r$ color evolution ($\Delta(g - r)/dt > 0.015 \text{ day}^{-1}$), or show only a modest flux increase when comparing the difference flux to the PSF flux in the ZTF reference image ($m_{\text{diff}} - m_{\text{ref}} > 1.5$). We also rejected all objects that can be classified as SNe or broad-line AGNs in our spectroscopic follow-up observations. The details of our photometric selection, including estimates for the completeness and selection effects which are required to compute event rates, will be presented in a forthcoming publication.

2.3. Discovery and Classification History

In Table 1, we list the IAU name, the ZTF name, our internal nickname,²² the name given by other optical transient surveys, and reference to the first public spectroscopic classification of this transient as a TDE. The table is sorted by the date of the first ZTF detection and credit for discovery of the transient, based on the first report to the Transient Name Server (TNS), is indicated using boldface.

Our TDE discovery pipeline does not use the TNS as input; we read and filter the ZTF alerts directly from their source (Patterson et al. 2019). The TNS reporting of ZTF alerts is mainly provided by AMPEL (Nordin et al. 2019) and by the Redshift Completeness Factor project (Fremling et al. 2020),

²² Given the seven-character length of the ZTF names required by the large volume of ZTF transient alerts, for ease of communication, we chose an internal naming scheme for our TDE candidates based on characters from the HBO TV show, Game of Thrones (GOT).

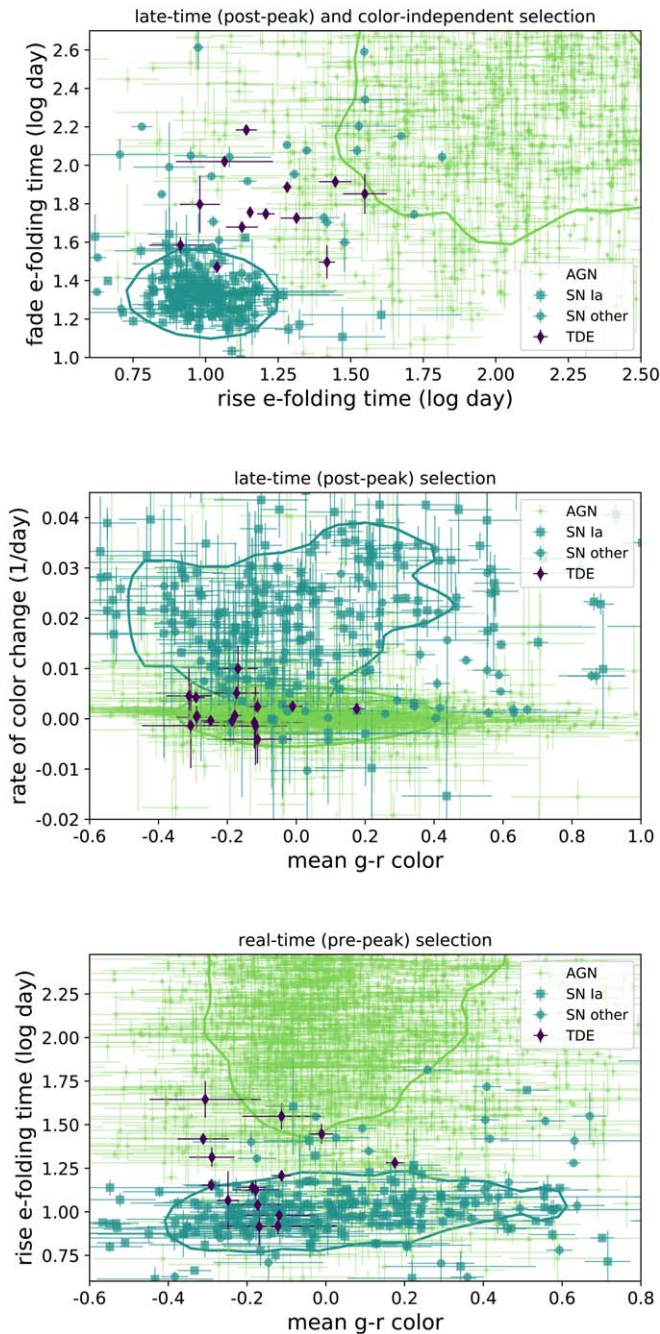


Figure 1. Yield of nuclear transients after 1.5 yr of ZTF observations. Contours enclose two-thirds of all spectroscopically classified nuclear supernovae (SNe) in our sample and two-thirds of the AGNs. The latter are classified based on archival data or prior variability. In the top panel, we see that TDEs have both longer rise times and a longer fading timescale compared to the majority of SNe. The middle panel demonstrates that color evolution provides further separation of TDEs from SNe. Here we display the mean $g - r$ color and the color change ($\Delta(g - r)/t$), both measured using all detections of the light curve. Tidal disruption flares show an almost constant optical color, while in postpeak observations most SNe show cooling (i.e., an increase of the color). For photometric selection of TDEs detected before maximum light, their blue color and slow rise time can be used (bottom panel), although this metric yields a larger background of SNe.

plus more recently by a filter implemented in the ALerCE broker. For 10 of the 17 sources in our sample, ZTF was the first survey to report a detection to TNS. As listed in Table 1, ATLAS provided three discoveries, ASAS-SN two discoveries, and Gaia and PS1 each claim one more discovery.

2.4. Spectroscopic Classification

In order to classify the TDEs into spectroscopic subclasses, we use the “best” spectrum, namely high signal-to-noise and prominent line features, for each of our TDEs from our various follow-up programs with the 4.3 m Discovery Channel Telescope De Veny Spectrograph (DCT/De Veny, PI: Gezari), the 200 inch Palomar Telescope Double Spectrograph (P200/DBSP, PI: Kulkarni), the 10 m Keck Low Resolution Imaging Spectrograph (Keck/LRIS, PI: Kulkarni), and the 3 m Lick Kast Double Spectrograph (Lick/Kast, PI: Foley). Spectra were reduced with PyRAF using standard long-slit spectroscopy data reduction procedures. For those spectra not corrected for telluric absorption, we show the spectra in Figure 2 with those wavelength regions masked out. In three cases, we use publicly available spectra from the TNS. In Table 2, we indicate the IAU name, date, phase in days since peak, and telescope and instrument of the spectrum we use for determining the spectroscopic subclassification shown in Figure 2, the TDE class, and the redshift. In all cases, the redshift is measured from host-galaxy absorption features.

We find that our ZTF TDE sample can be divided into three spectroscopic classes:

1. *TDE-H*: broad $H\alpha$ and $H\beta$ emission lines.
2. *TDE-H+He*: broad $H\alpha$ and $H\beta$ emission lines and a broad complex of emission lines around $\text{He II } \lambda 4686$. The majority of the sources in this class also show $\text{N III } \lambda 4640$ and emission at $\lambda 4100$ (identified as $\text{N III } \lambda 4100$ instead of $H\delta$), plus and in some cases also $\text{O III } \lambda 3760$.
3. *TDE-He*: no broad Balmer emission lines, a broad emission line near $\text{He II } \lambda 4686$ only.

In our flux-limited sample of TDEs with ZTF observations, the relative ratios of the classes are $\text{H:H+He:He} = 8:7:1$. In Section 7, we will elaborate on how the rarity of the TDE-He class might be an important clue to understand what conditions are needed to provide the spectroscopic properties of TDEs. Two of the TDEs (AT2019meg and AT2019dsg) also have strong narrow emission lines from star formation in their host galaxies.

These classifications are based on a single spectral epoch obtained near the peak of the flare. There is at least one case in which a TDE showed the late-time disappearance of $H\alpha$ emission (Nicholl et al. 2019a), which according to our classification scheme, would result in a change of spectral class from TDE-H+He to TDE-He.

A detailed analysis of the spectroscopic evolution of the ZTF TDEs and their line features with time will be presented in a future paper (T. Hung et al. 2021, in preparation). For one of our TDEs, AT2019eve, a follow-up spectrum obtained 6 months after peak, demonstrated the appearance of strong, narrow He I lines, potentially a signature of a Type Ibn SN (although the presence of strong Balmer lines is inconsistent with this classification). We therefore label the spectral class of AT2019eve as “Unknown” until more careful analysis of the host-galaxy contribution to the emission-line spectrum. We note also that the rise time of the flare and the blackbody temperature are also outliers compared to the rest of the TDEs in our sample, the blackbody temperature of AT2019eve is below the threshold for TDE identification established by van Velzen et al. (2020).

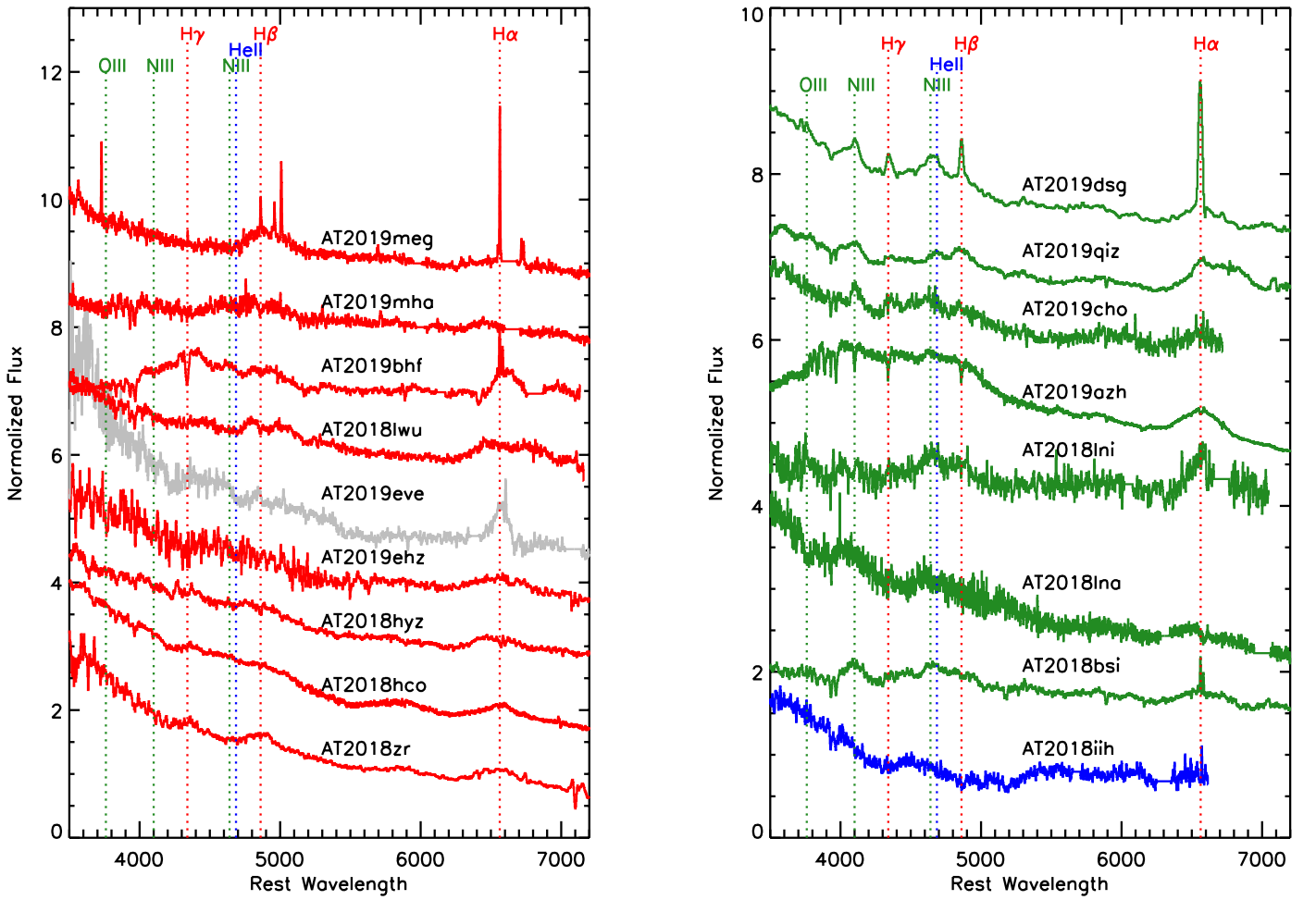


Figure 2. Spectroscopic classifications of our ZTF TDE sample from medium-resolution spectroscopy. Left: TDEs with Balmer line features only (TDE-H, in red). Right: TDEs with Balmer lines and a broad emission feature at He II (TDE-H+He, in green), and TDEs with only He II emission (TDE-He, in blue). Spectra have not been host galaxy subtracted.

Table 2
Spectroscopic Observations and TDE Classification

IAU Name	Date	Phase	Telescope/Inst.	TDE Class	Redshift	ID
AT2018zr	2018 Mar 28	25	WHT/ISIS ^a	TDE-H	0.071	1
AT2018bsi	2018 May 13	34	DCT/De Veny	TDE-H+He	0.051	2
AT2018hco	2018 Nov 10	29	Keck/LRIS	TDE-H	0.088	3
AT2018iuh	2019 Mar 10	102	DCT/De Veny	TDE-He	0.212	4
AT2018hyz	2018 Nov 12	6	FTN/Floyds-N ^b	TDE-H	0.0458	5
AT2018Ini	2019 Mar 1	81	DCT/De Veny	TDE-H+He	0.138	6
AT2018Ina	2019 Jan 26	0	Palomar/DBSP	TDE-H+He	0.091	7
AT2019cho	2019 May 2	58	DCT/De Veny	TDE-H+He	0.193	8
AT2019bhf	2019 May 29	90	DCT/De Veny	TDE-H	0.1206	9
AT2019azh	2019 May 1	46	Keck/LRIS	TDE-H+He	0.0222	10
AT2019dsg	2019 May 13	13	NTT/EFOSC2 ^c	TDE-H+He	0.0512	11
AT2019ehz	2019 Jun 14	35	Lick/Kast	TDE-H	0.074	12
AT2019eve	2019 Jun 29	50	DCT/De Veny	Unknown	0.0813	13
AT2019mha	2019 Aug 27	17	Palomar/DBSP	TDE-H	0.148	14
AT2019meg	2019 Aug 10	8	Palomar/DBSP	TDE-H	0.152	15
AT2019lwu	2019 Aug 27	31	DCT/De Veny	TDE-H	0.117	16
AT2019qiz	2019 Nov 5	29	DCT/De Veny	TDE-H+He	0.0151	17

Notes.

^a Spectrum published in Hung et al. (2019).

^b Publicly available spectrum on TNS posted by Dong et al. (2018).

^c Publicly available spectrum on TNS posted by Nicholl et al. (2019b).

3. Host-galaxy Properties

The stellar mass of the TDE host galaxies is estimated from the preflare photometry of the host. For most of our sources, no preflare spectroscopic observations of the host are available, and the redshift is obtained from the spectrum of the TDE. We use SDSS model magnitudes (Stoughton et al. 2002) or Pan-STARRS Kron magnitudes (Chambers et al. 2016) for sources outside the SDSS footprint. For the handful of sources outside the Pan-STARRS footprint, we use the Dark Energy Camera Legacy Survey (DECaLS; Dey et al. 2019) or SkyMapper (Wolf et al. 2018) observations. We also include GALEX NUV and FUV photometry (Martin et al. 2005), both detections or upper limits. For AT2018dyb, we use the host photometry provided by Holoien et al. (2020).

To obtain a posterior distribution for parameters of the flexible stellar population synthesis (FSPS; Conroy et al. 2009) module we use the Prospector (Johnson & Leja 2017) software to run a Markov Chain Monte Carlo (MCMC) sampler (Foreman-Mackey et al. 2013). We adopted the same model choices that were used by Mendel et al. (2014), who applied the FSPS module to the SDSS galaxy sample. The five free parameters are the stellar mass, the Calzetti et al. (2000) dust model optical depth, the age of the stellar population, the metallicity (Z), and the e-folding time of the star formation history (τ_{sfh}). We use flat priors over the same parameter range as Mendel et al. (2014). Sufficient sampling of the posterior is ensured by using only the second half of 1000 steps, taken by 100 walkers.

Figure 3 shows the extinction-corrected, synthetic rest-frame $u - r$ color versus total stellar mass for the TDE host galaxies from the stellar population synthesis fits to the preflare spectral energy distributions (SEDs) described above, together with a sample of approximately 17,000 comparison galaxies from SDSS with observed $u - r$ colors. Figure 3 also shows the sample of known TDEs listed in Table 3 with the same comparison sample of SDSS galaxies. This comparison sample is based on the Mendel et al. (2014) value added catalog of bulge, disk, and total stellar mass estimates. This catalog contains spectroscopically classified galaxies (Strauss et al. 2002), with mass estimates based on FSPS (i.e., the same software we used for the TDE host galaxies).

In Figure 4, we show cutouts of the host-galaxy color gri images from SDSS (or Pan-STARRS1 when SDSS is not available) for the 17 ZTF TDE galaxy hosts, in order of increasing redshift. The morphology of the host galaxies appears to be dominated by an elliptical component, typically for early-type galaxies; some of the lowest redshift TDE hosts ($z = 0.015\text{--}0.05$) show a compact core and an extended spiral and/or disk structure.

The magnitude limit of the ZTF imaging data ($m \approx 23$ for the coadd) is deeper than the magnitude limit of SDSS spectroscopic galaxy sample ($m < 17.77$, Strauss et al. 2002). Our highest redshift TDE with ZTF observations is at $z = 0.21$, which implies a nuclear transient search with ZTF is sensitive to a volume-complete sample of galaxies with $M_r \lesssim -18$. To match this absolute magnitude limit, we restrict the comparison catalog of spectroscopic galaxies from SDSS by applying a redshift cut of $z < 0.04$. We have indicated the location of the green valley in Figure 3, as originally defined in Schawinski et al. (2014). However, as our sample has a different redshift cut, we have redefined the upper bound of the green valley

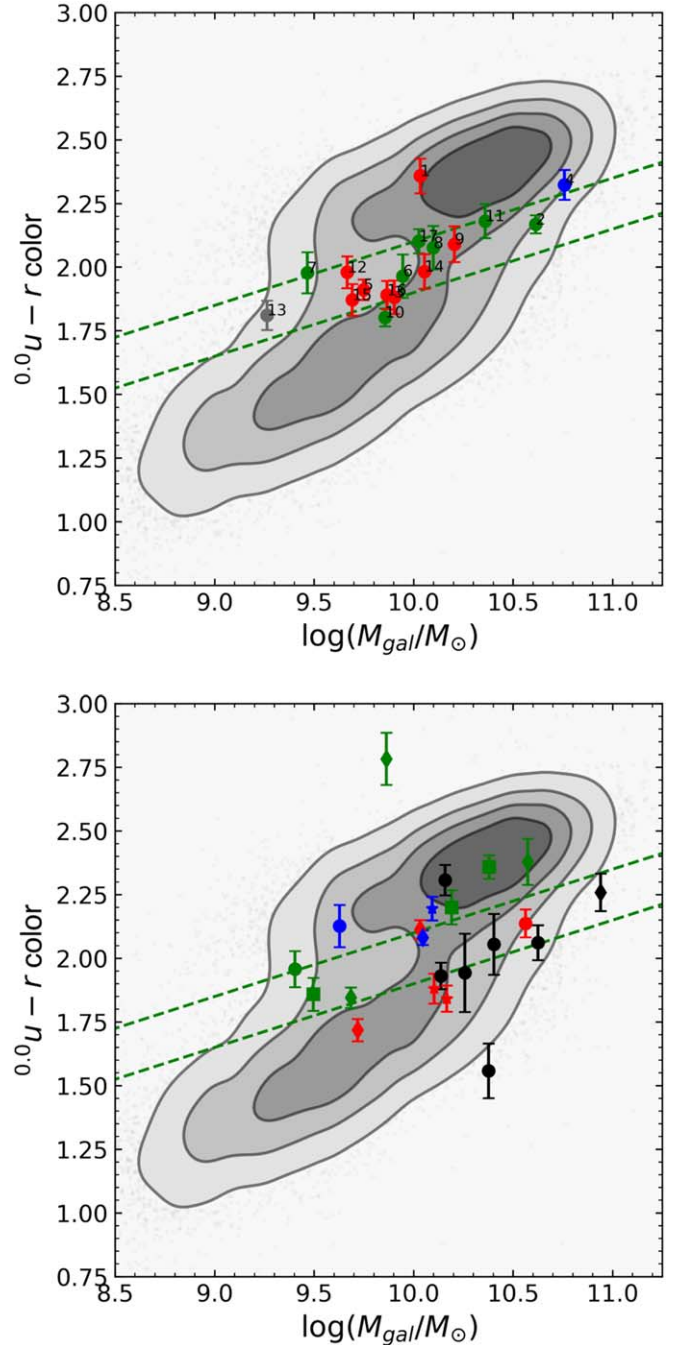


Figure 3. The extinction-corrected rest-frame $u - r$ color and the total stellar mass, both obtained from the best-fit population synthesis model. In the top panel, we show the 17 TDE host galaxies (labeled by their corresponding number in the ID column of Table 2). In the bottom, we show known TDEs from the literature (Table 3), with diamonds indicating ASAS-SN sources, squares for iPTF sources, stars for PTF sources, and dots for the remaining surveys. Colors of symbols correspond to the spectral classifications given in Tables 2 and 3, with TDE-H in red, TDE-H+He in green, TDE-He in blue, and either unclassified or unknown in black. The contours enclose a volume-limited comparison sample of galaxies, matched to the depth of ZTF, decreasing in steps of 0.5σ to 2σ for the outer contour. We see that host galaxies in the green valley are significantly overrepresented in both samples.

based on our galaxy distribution:

$${}^{0.0}u - r(M_{\text{gal}}) = -0.40 + 0.25 \times M_{\text{gal}} \quad (1)$$

but kept the width of the green valley fixed to that of Schawinski et al. (2014), of 0.2 mag, to define the lower bound.

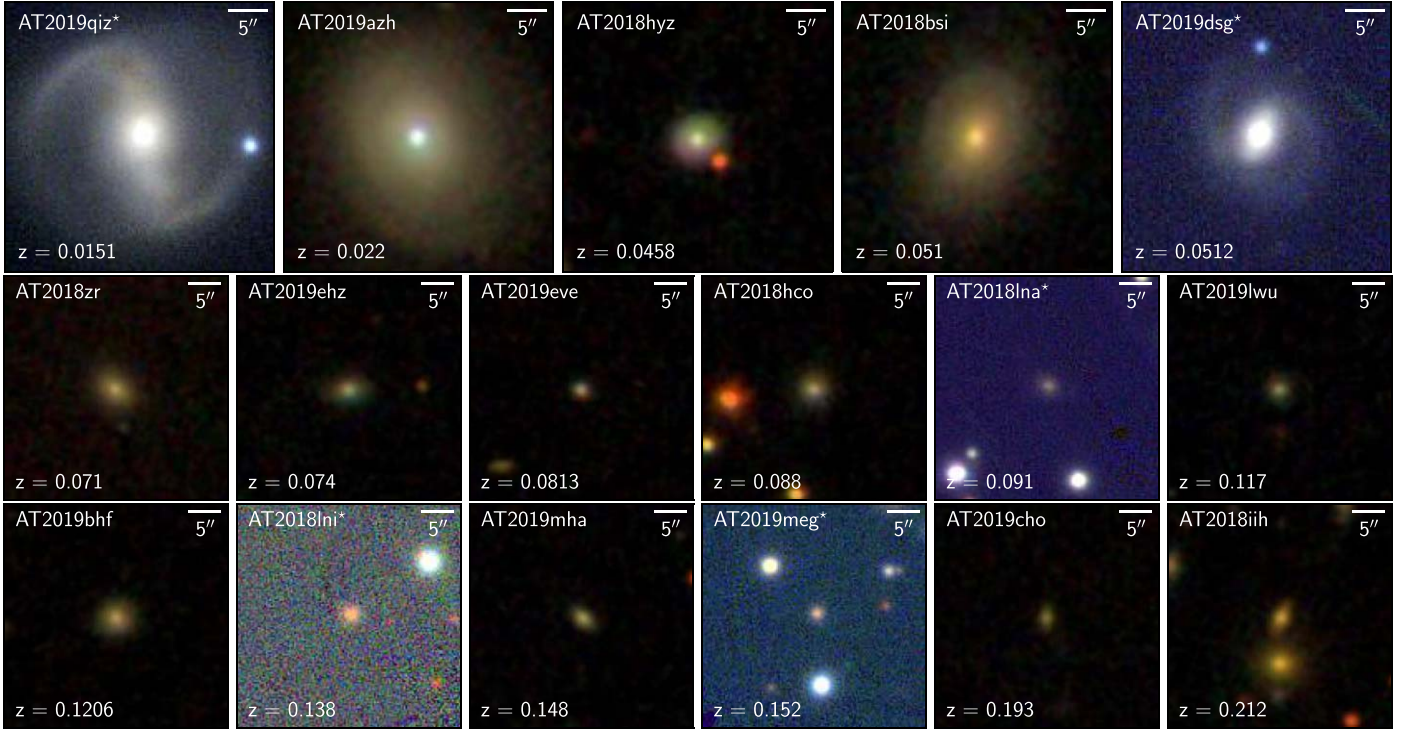


Figure 4. SDSS *gri* images of the TDE host galaxies in order of increasing redshift. Galaxies with a star next to the name are not in the SDSS footprint and therefore have Pan-STARRS *gri* images. All images are $34'' \times 34''$.

Table 3
Known TDEs Included in Population Analysis

Discovery Name/IAU Name	References	Spectral Type	z
GALEX-D1-9	1	No spectrum	0.316
GALEX-D3-13	2	No spectrum	0.3698
GALEX-D23H-1	2	No spectrum	0.1855
SDSS-TDE1	3	No spectrum	0.136
SDSS-TDE2	3	TDE-H	0.256
PS1-10jh	4	TDE-He	0.1696
PS1-11af	5	Unknown	0.4046
PS17dhz/AT2017eqx	6	TDE-H+He	0.1089
PTF-09ge	7	TDE-He	0.064
PTF-09axc	7	TDE-H	0.1146
PTF-09djl	7	TDE-H	0.184
ASASSN-14ae	8	TDE-H	0.0436
ASASSN-14li	9	TDE-H+He	0.0205
ASASSN-15oi	10	TDE-He	0.0484
ASASSN-15lh	11	Unknown	0.2316
ASASSN-18pg/AT2018dyb	12	TDE-H+He	0.018
ASASSN-18ul/AT2018fyk	13	TDE-H+He	0.059
ASASSN-19bt/AT2019ahk	14	TDE-H	0.0262
iPTF-15af	15	TDE-H+He	0.0789
iPTF-16axa	16	TDE-H+He	0.108
iPTF-16fnl	17	TDE-H+He	0.0163
OGLE16aaa	18	Unknown	0.1655

References. (1) Gezari et al. (2006); (2) Gezari et al. (2008); (3) van Velzen et al. (2011); (4) Gezari et al. (2012); (5) Chornock et al. (2014); (6) Nicholl et al. (2019a); (7) Arcavi et al. (2014); (8) Holoien et al. (2014); (9) Holoien et al. (2016b); (10) Holoien et al. (2016a); (11) Dong et al. (2016); (12) Leloudas et al. (2019); (13) Wevers et al. (2019a); (14) Holoien et al. (2019a); (15) Blagorodnova et al. (2019); (16) Hung et al. (2017); (17) Blagorodnova et al. (2017); (18) Wyrzykowski et al. (2017).

The ZTF sample of TDE host galaxies is dominated by green valley galaxies (Figure 3), with $\approx 65\%$ of the TDE hosts falling within the limits of the green valley region compared to 13% of the SDSS comparison sample. Law-Smith et al. (2017) used the definition of the green valley based on total star formation rate and found that their sample of TDE host galaxies may be transitioning from star-forming to quiescent, a time during which quenching of star formation causes galaxies to cross into the green valley (Schawinski et al. 2014). The green valley is also known to host quiescent, Balmer-strong galaxies (including post-starburst or E+A galaxies), which previous studies have shown to be overrepresented in TDE host-galaxy populations (Arcavi et al. 2014; French et al. 2016; Law-Smith et al. 2017; Graur et al. 2018). Late-time spectra of the ZTF host galaxies can be used to obtain better star formation rate estimates, but these are not yet available for the entire sample (in some cases the flare still dominates the optical emission).

The host-galaxy population synthesis for the ZTF sources is provided in a `tar.gz` package. The package contains 17 JSON tables and a Python script to read them. Each table has the same information given in Table 4 along with the galaxy flux in various filters and its extinction.

4. Follow-up Observations

4.1. Optical: SEDM and LT

For a few TDEs, we acquired multiband images with P60/SEDM (Blagorodnova et al. 2018; Rigault et al. 2019) and/or the optical imager (IO:O) on the Liverpool Telescope (LT; Steele et al. 2004). For LT data, image reductions were provided by the IO:O pipeline. For both LT and SEDM, image subtraction was performed versus PS1 (*g*, *r*, *i*, *z* bands) or

Table 4
Host Properties

Name	Mass log M_{\odot}	$^{0.0}_u - r$	Dust $E(B - V)$	Age Gyr	τ_{sfb} Gyr	Z/Z_{\odot} log
AT2018zr	10.03 $^{0.09}_{0.18}$	2.36 $^{0.05}_{0.08}$	0.09 $^{0.16}_{0.07}$	6.56 $^{2.35}_{3.07}$	0.22 $^{0.25}_{0.09}$	-0.19 $^{0.15}_{0.25}$
AT2018bsi	10.61 $^{0.05}_{0.06}$	2.17 $^{0.03}_{0.04}$	0.75 $^{0.14}_{0.17}$	2.67 $^{0.89}_{0.58}$	0.59 $^{0.23}_{0.15}$	-0.27 $^{0.21}_{0.25}$
AT2018hco	9.90 $^{0.09}_{0.18}$	1.88 $^{0.06}_{0.07}$	0.26 $^{0.23}_{0.20}$	5.25 $^{2.62}_{2.79}$	0.29 $^{0.40}_{0.15}$	-1.48 $^{0.54}_{0.39}$
AT2018iih	10.76 $^{0.09}_{0.15}$	2.32 $^{0.05}_{0.07}$	0.29 $^{0.40}_{0.21}$	7.10 $^{3.33}_{3.11}$	0.25 $^{0.30}_{0.12}$	-0.59 $^{0.44}_{0.46}$
AT2018hyz	9.75 $^{0.12}_{0.26}$	1.91 $^{0.05}_{0.03}$	0.28 $^{0.14}_{0.15}$	3.95 $^{1.73}_{2.43}$	0.18 $^{0.20}_{0.07}$	-1.08 $^{0.73}_{0.54}$
AT2018lni	9.94 $^{0.10}_{0.15}$	1.97 $^{0.09}_{0.08}$	0.53 $^{0.30}_{0.36}$	4.49 $^{4.53}_{1.95}$	0.28 $^{0.37}_{0.14}$	-1.56 $^{0.51}_{0.31}$
AT2018lna	9.47 $^{0.12}_{0.09}$	1.98 $^{0.09}_{0.07}$	0.20 $^{0.19}_{0.13}$	6.55 $^{3.92}_{2.19}$	0.31 $^{0.35}_{0.22}$	-1.24 $^{0.40}_{0.55}$
AT2019cho	10.10 $^{0.17}_{0.16}$	2.08 $^{0.10}_{0.07}$	0.33 $^{0.33}_{0.23}$	5.13 $^{5.32}_{2.62}$	0.39 $^{0.41}_{0.22}$	-0.87 $^{0.72}_{0.66}$
AT2019bhf	10.21 $^{0.15}_{0.12}$	2.09 $^{0.06}_{0.08}$	0.72 $^{0.20}_{0.36}$	3.20 $^{1.97}_{1.17}$	0.45 $^{0.35}_{0.26}$	-0.99 $^{0.61}_{0.65}$
AT2019azh	9.86 $^{0.15}_{0.14}$	1.80 $^{0.03}_{0.04}$	0.39 $^{0.11}_{0.13}$	2.32 $^{1.07}_{0.94}$	0.17 $^{0.18}_{0.05}$	-1.34 $^{0.69}_{0.41}$
AT2019dsg	10.36 $^{0.17}_{0.12}$	2.18 $^{0.05}_{0.08}$	0.43 $^{0.30}_{0.31}$	4.99 $^{4.87}_{1.85}$	0.52 $^{0.30}_{0.32}$	-0.76 $^{0.51}_{0.74}$
AT2019ehz	9.67 $^{0.09}_{0.15}$	1.98 $^{0.06}_{0.06}$	0.22 $^{0.21}_{0.15}$	5.59 $^{3.02}_{2.34}$	0.25 $^{0.31}_{0.12}$	-1.15 $^{0.41}_{0.51}$
AT2019eve	9.26 $^{0.11}_{0.17}$	1.81 $^{0.06}_{0.05}$	0.24 $^{0.41}_{0.16}$	5.26 $^{3.06}_{2.97}$	0.38 $^{0.37}_{0.23}$	-1.67 $^{0.54}_{0.23}$
AT2019mha	10.05 $^{0.11}_{0.15}$	1.98 $^{0.06}_{0.07}$	0.53 $^{0.19}_{0.30}$	3.46 $^{2.51}_{1.27}$	0.30 $^{0.33}_{0.15}$	-1.38 $^{0.50}_{0.37}$
AT2019meg	9.66 $^{0.07}_{0.07}$	1.87 $^{0.08}_{0.08}$	0.57 $^{0.30}_{0.35}$	2.55 $^{0.87}_{0.73}$	0.73 $^{0.19}_{0.22}$	-0.39 $^{0.42}_{0.44}$
AT2019lwu	9.87 $^{0.12}_{0.15}$	1.89 $^{0.06}_{0.05}$	0.12 $^{0.20}_{0.09}$	5.68 $^{3.88}_{2.13}$	0.26 $^{0.32}_{0.13}$	-1.34 $^{0.45}_{0.44}$
AT2019qiz	10.03 $^{0.10}_{0.14}$	2.10 $^{0.05}_{0.05}$	0.33 $^{0.24}_{0.22}$	6.18 $^{3.53}_{2.53}$	0.24 $^{0.34}_{0.11}$	-0.96 $^{0.23}_{0.47}$

SDSS (u band) reference imaging, following the techniques of Fremling et al. (2016). PSF photometry was performed relative to PS1/SDSS photometric standards.

4.2. UV: *Swift*/UVOT

All of our 17 ZTF TDEs have Neil Gehrels Swift Observatory (Gehrels et al. 2004) follow-up observations in the UV and X-ray from UVOT (Romig et al. 2005) and XRT (Burrows et al. 2005), respectively, with a typical cadence of 3–5 days, and in most cases triggered within 2 weeks of the peak. Some of the fainter TDEs have only a few epochs of Swift observations, but they are sufficient to measure the average temperature of the UV/optical component, given that the optical colors of these TDEs are relatively constant with time.

The Swift photometry was measured using the `uvotsource` package with an aperture of $5''$, in the AB system, and corrected for the enclosed energy within the aperture (for AT2019azh, AT2018bsi, and AT2019dsg, we use a larger aperture to make sure we capture all the flux of the host galaxy). We estimate the host-galaxy flux in the UVOT bandpass from the posterior distribution of the population synthesis models. The uncertainty on this baseline level is propagated into our measurement of the TDE flux. Our host-subtracted UVOT aperture photometry, as well as the ZTF, SEDM, and LT photometry, is displayed in Figure 5 and the data is available online.

4.3. X-Ray: *Swift*/XRT

The 0.3–10 keV X-ray light curves for the four TDEs with XRT detections were produced using the UK Swift Data center online XRT data products tool, which uses the HEASOFT v6.22 software (Arnaud 1996). We used a fixed aperture at the ZTF coordinate of the transient and converted to flux using the best-fit blackbody model to the stacked XRT spectrum. The XRT stacked spectra were processed by the XRT Products Page (Evans et al. 2009), with Galactic extinction fixed to values from the HI4PI survey (HI4PI Collaboration et al. 2016): $N_{\text{H}}/10^{20} \text{ cm}^{-2} = 2.59, 6.46, 1.42$, and 4.16 , for AT2018hyz, AT2019dsg, AT2019ehz, and AT2019azh, respectively. The resulting temperatures are $kT/$

keV = 0.131 ± 0.026 , 0.071 ± 0.003 , 0.101 ± 0.004 , and 0.053 ± 0.001 , again for AT2018hyz, AT2019dsg, AT2019ehz, and AT2019azh, respectively (uncertainties correspond to the 90% confidence levels). These soft blackbody temperatures are similar to the previously known X-ray-detected optically selected TDEs: ASASSN-14li ($kT = 0.050$ keV; Miller et al. 2015), ASASSN-15oi ($kT = 0.045$ keV; Gezari et al. 2017), AT2018zr/PS18kh ($kT = 0.10$ keV; van Velzen et al. 2019e), and AT2018fyk/ASASSN-18ul ($kT = 0.12$ keV; Wevers et al. 2019b).

Finally, we note that, while this paper was under review, a fifth source in our sample, AT2019qiz, was shown to yield a significant detection of X-ray photons when multiple XRT observations are binned together (Nicholl et al. 2020).

5. Light-curve Analysis

We extract the properties of the light curve by fitting a model to the data from ZTF, Swift/UVOT, and if available, LT and SEDM. We also include known TDEs from the literature, selecting all sources used in the luminosity function analysis of van Velzen (2018) as well as spectroscopically confirmed TDEs that have been published since. We use the published photometry and our own analysis of the public Swift/UVOT data (see Section 4.2). We add all TDEs listed in Table 3 to obtain a total of 39 sources (this final sample includes four sources with a spectrum of the flare that are classified as Unknown, and four sources without a spectrum of the flare.)

5.1. Light-curve Model

We consider two models to describe the TDE light curve. First, for the first 100 days after maximum light, we use a Gaussian rise and exponential decay:

$$L_{\nu}(t) = L_{\nu_0 \text{ peak}} \frac{B_{\nu}(T_0)}{B_{\nu_0}(T_0)} \times \begin{cases} e^{-(t-t_{\text{peak}})^2/2\sigma^2} & t \leq t_{\text{peak}} \\ e^{-(t-t_{\text{peak}})/\tau} & t > t_{\text{peak}} \end{cases} \quad (2)$$

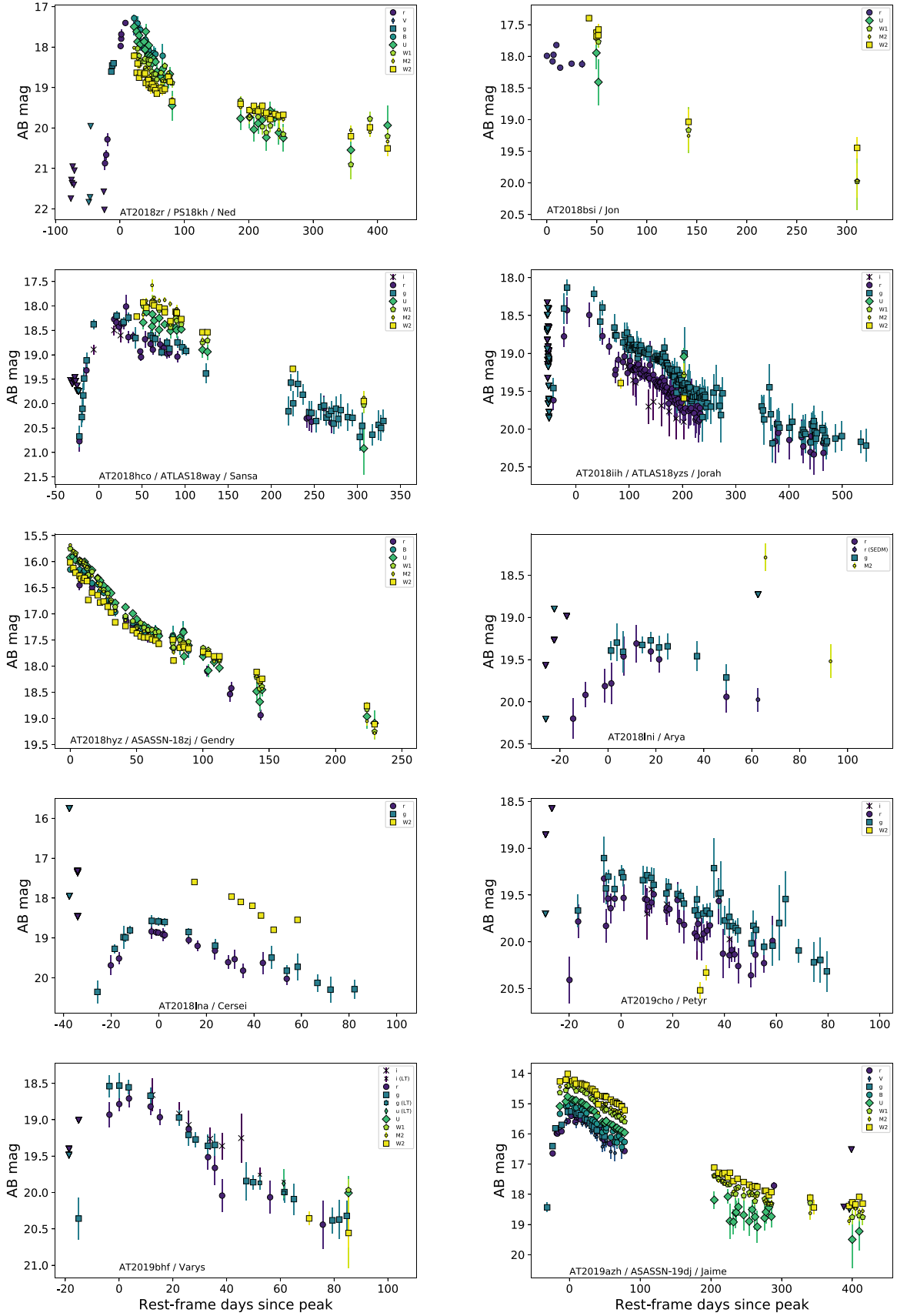


Figure 5. Optical/UV light curves based on ZTF, Swift/UVOT, SEDM, and LT photometry. Arrows indicate 5σ upper limits, based on the ZTF alert photometry. (The data used to create this figure are available.)

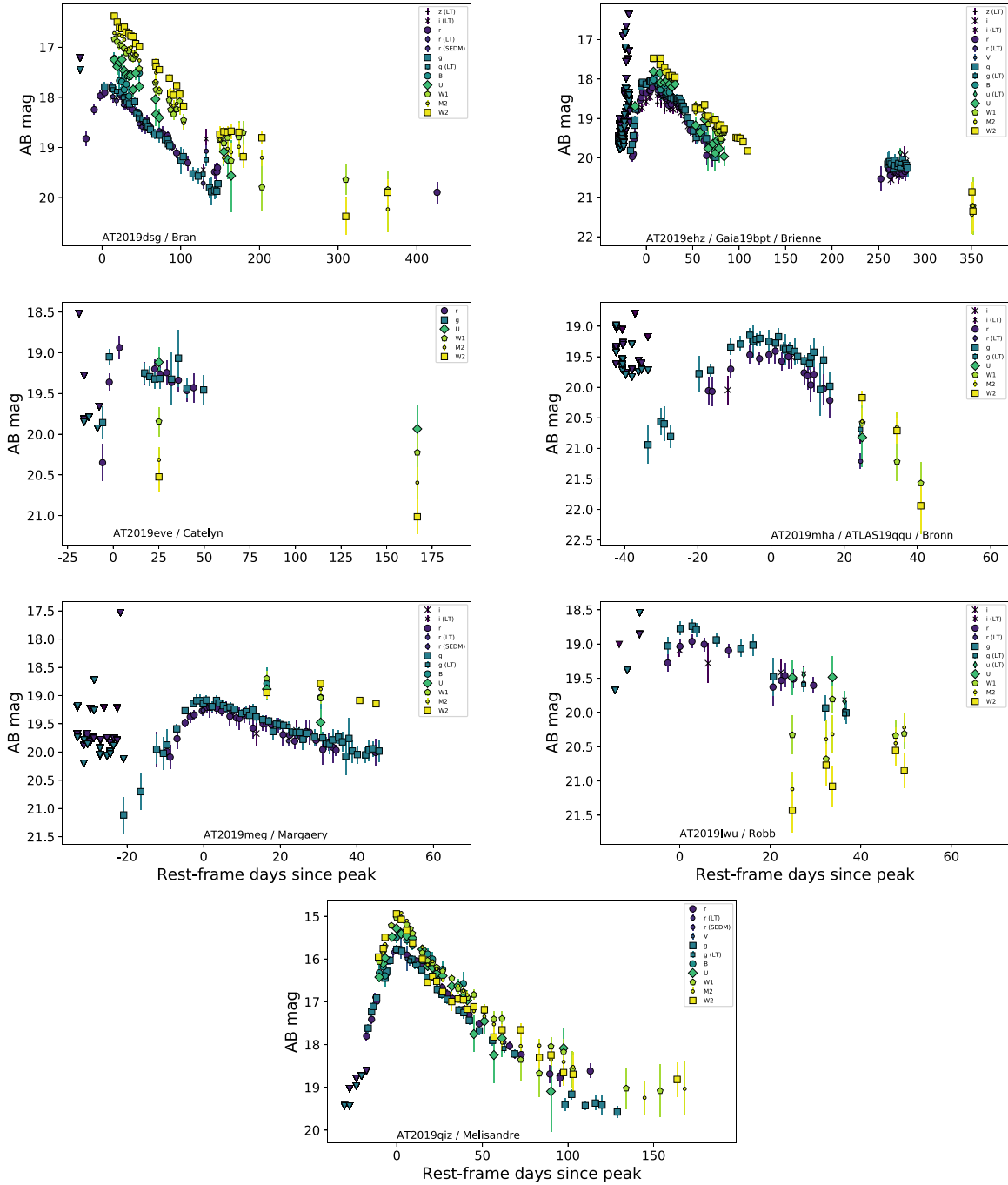


Figure 5. (Continued.)

Here, $L_{\nu_0 \text{ peak}}$ is the peak luminosity, measured at the reference frequency ν_0 (in the rest frame of the source). To predict the luminosity in other bands, we assume the spectrum follows a blackbody, $B_\nu(T_0)$, with a constant temperature T_0 . We pick the g band (6.3×10^{14} Hz) as our reference frequency. We adopt T_0 as our default temperature measurement, and we use this temperature to estimate the peak bolometric luminosity (L_{bb}) and blackbody radius (R).

One advantage of Equation (2) is simplicity: measuring the rise/decay timescale independently with multiband observations would not be possible with fewer free parameters. However, for observations longer than 100 days, all TDEs show deviations

from an exponential decay. A power law is required to properly describe the light curve, and this introduces an extra free parameter. In our second light-curve model, we therefore use a power-law decay and also allow for evolution of the blackbody temperature:

$$L(t, \nu) = L_{\text{peak}} \frac{\pi B_\nu(T(t))}{\sigma_{\text{SB}} T^4(t)} \times \begin{cases} e^{-(t-t_{\text{peak}})^2/2\sigma^2} & t \leq t_{\text{peak}} \\ [(t - t_{\text{peak}} + t_0)/t_0]^p & t > t_{\text{peak}} \end{cases} \quad (3)$$

Here σ_{SB} is the Stephan–Boltzmann constant. While this model allows for temperature evolution, we cannot measure this at the

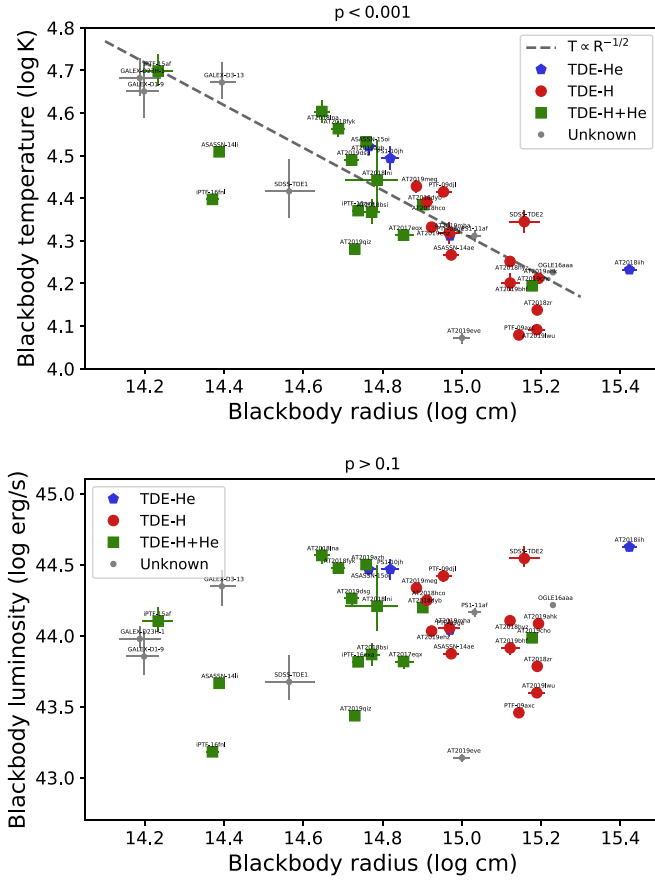


Figure 6. Blackbody temperature and blackbody luminosity vs. the blackbody radius, all measured at the peak of the TDE light curve. In the top panel, the dashed line shows the relation expected for a single blackbody spectrum with a luminosity of $10^{44.1}$ erg s $^{-1}$. We see that the TDE-H+He class has smaller radii and larger temperatures compared to the other two spectroscopic TDE classes. There is no difference in the blackbody luminosity of the TDE-H+He and TDE-H class, but the TDE-He class appears to have a higher average luminosity.

same cadence as the observations because (1) the Swift and ZTF observations were not obtained simultaneously, and (2) the uncertainty on the temperature estimated from a single epoch are often very large. We therefore first try a simple linear relation for the postpeak temperature evolution:

$$T(t) = (T_0) + dT/dt \times (t - t_{\text{peak}}). \quad (4)$$

Here, dT/dt is a free parameter with units K day $^{-1}$, and we use a flat prior with $10^4 < T/K < 10^5$. This simple model works well for most TDEs, because they only show very modest temperature evolution (about 50 K day $^{-1}$, which corresponds to a 20% increase over 100 days; see Figure 6).

However, for some sources, more rapid temperature changes have been observed (e.g., Holoien et al. 2018), and to allow for more flexibility in our description of temperature evolution, we use a linear interpolation of the temperature on a grid of fixed points in time. The points on this grid are the free parameters of our fit. The grid starts at the time of the peak, and the spacing is ± 30 days. At each grid point, we use a log-normal Gaussian prior with a dispersion of 0.1 dex centered on the best-fit mean temperature from our simplest light-curve model (Equation (2)). We adopt this nonparametric approach as our default model to estimate the parameters of the power law (p , and t_0) as well as the rise timescale.

Table 5

Priors for MCMC Light-curve Analysis

Parameter	Description	Prior
$\log L_{\text{peak}}$	Peak luminosity	$[L_{\text{max}}/2, 2L_{\text{max}}]^a$
t_{peak}	Time of peak	$[-20, 20]$ days ^a
$\log T_0$	Mean temperature	$[4, 5]$ K
$\log \sigma$	Gaussian rise time	$[0, 1.5]$ days
$\log \tau$	Exponential decay time	$[0, 3]$ days
p	Power-law index	$[-5, 0]$
$\log t_0$	Power-law normalization	$[0, 3]$ days
dT/dt	Temperature change	$[-200, 200]$ K day $^{-1}$
$\ln(f)$	White noise factor	$[-5, -1.8]$

Note.

^a $L(t=0) \equiv L_{\text{max}}$ is the observed maximum luminosity. When we fit for the blackbody luminosity (Equation (3)), we compute L_{max} using the mean temperature measured for the first 100 days since peak (i.e., T_0 as obtained from fitting Equation (2)).

We apply our single power-law decay model (Equation (3)) only to the first year of data (measured after maximum light) because at later times, many TDE light curves show significant flattening that is not consistent with the early-time power-law decay (van Velzen et al. 2019c), likely due to the contribution of an accretion disk to the optical/UV light.

5.1.1. Light-curve Parameter Inference

To estimate the parameters of our two models we use the emcee sampler (Foreman-Mackey et al. 2013). Following van Velzen et al. (2019c), we use a Gaussian likelihood function that includes a “white-noise” term, $\ln(f)$, which allows for additional variance in the data that is not captured by the reported measurement uncertainty. We use 100 walkers and 2000 steps, discarding the first 1500 steps to ensure convergence. We use a flat prior for all parameters (except for the grid points that anchor the temperature evolution): the boundaries of the parameters are listed in Table 5.

An exception is made for sources with no detections prior to maximum light, i.e., TDEs discovered postpeak. For these, we force $t_{\text{peak}} = 0$ when measuring L_{peak} using Equation (2). However, we always use the default priors (Table 5) when estimating the best-fit parameters of the power-law decay (Equation (3)), because this allows the uncertainty on the true time of peak to enter the posterior distributions of the power-law parameters. Finally, we also make an exception for the three TDEs from PTF (Table 3). These are the only sources with light curves that have no UV coverage in the first year, and we therefore keep their blackbody temperature fixed at the value measured from the optical spectrum by Arcavi et al. (2014).

To estimate the blackbody radius and blackbody luminosity at peak, we sample the posterior distribution of T_0 and L_{peak} as obtained from the model of Equation (2). For all parameters, the reported uncertainty follows from a credible interval of $[0.16, 0.84]$, i.e., $\pm 1\sigma$ for Gaussian statistics.

The ZTF light curve of two sources in our sample was included in the reference image, hence the IPAC difference-imaging light curves are compromised and excluded from the light-curve analysis. In one case (AT2018bsi), both r -band and g -band light curves are affected, but we were able to use alerts based on an earlier, TDE-free, r -band reference frame that had been created during the ZTF commission period. For the

Table 6
Light-curve Shape Parameters

Name	L_g log erg s ⁻¹	L_{bb} log erg s ⁻¹	T log K	dT/dt 10 ² K day ⁻¹	$t_{peak/max}$ MJD	σ log day	τ log day	p	t_0 log day	$t_0 _{p=-5/3}$ log day
AT2018zr	43.44 ^{+0.02} _{-0.02}	43.78 ^{+0.02} _{-0.02}	4.14 ^{+0.01} _{-0.01}	0.46 ^{+0.05} _{-0.05}	58180.7 ^{+1.1} _{-1.0}	1.0 ^{+0.04} _{-0.03}	1.88 ^{+0.03} _{-0.03}	-0.8 ^{+0.0} _{-0.1}	1.23 ^{+0.15} _{-0.12}	2.14 ^{+0.03} _{-0.03}
AT2018bsi	43.08 ^{+0.03} _{-0.03}	43.87 ^{+0.08} _{-0.08}	4.37 ^{+0.03} _{-0.03}	0.21 ^{+0.63} _{-0.30}	58217.2	...	1.94 ^{+0.12} _{-0.10}	-1.9 ^{+0.4} _{-0.6}	1.92 ^{+0.25} _{-0.21}	1.83 ^{+0.09} _{-0.07}
AT2018hco	43.41 ^{+0.02} _{-0.02}	44.25 ^{+0.04} _{-0.04}	4.39 ^{+0.01} _{-0.01}	0.05 ^{+0.10} _{-0.09}	58401.8 ^{+1.7} _{-1.9}	0.9 ^{+0.04} _{-0.04}	2.03 ^{+0.04} _{-0.04}	-1.2 ^{+0.2} _{-0.2}	1.73 ^{+0.16} _{-0.15}	2.00 ^{+0.06} _{-0.07}
AT2018iih	44.15 ^{+0.03} _{-0.03}	44.62 ^{+0.04} _{-0.03}	4.23 ^{+0.01} _{-0.01}	0.19 ^{+0.05} _{-0.05}	58442.2 ^{+1.6} _{-0.8}	1.2 ^{+0.01} _{-0.01}	2.05 ^{+0.04} _{-0.04}	-0.9 ^{+0.1} _{-0.1}	1.61 ^{+0.11} _{-0.07}	2.06 ^{+0.06} _{-0.05}
AT2018hyz	43.56 ^{+0.01} _{-0.01}	44.1 ^{+0.01} _{-0.01}	4.25 ^{+0.01} _{-0.01}	0.18 ^{+0.05} _{-0.05}	58428.0	...	1.72 ^{+0.01} _{-0.01}	-1.1 ^{+0.1} _{-0.1}	1.29 ^{+0.07} _{-0.06}	1.71 ^{+0.01} _{-0.01}
AT2018lni	43.26 ^{+0.03} _{-0.03}	44.21 ^{+0.29} _{-0.17}	4.44 ^{+0.09} _{-0.07}	0.48 ^{+0.46} _{-0.47}	58460.3 ^{+3.6} _{-3.8}	0.8 ^{+0.18} _{-0.12}	2.16 ^{+0.16} _{-0.12}	-1.4 ^{+0.8} _{-1.6}	2.46 ^{+0.37} _{-0.45}	2.23 ^{+0.22} _{-0.19}
AT2018lna	43.22 ^{+0.02} _{-0.02}	44.56 ^{+0.06} _{-0.06}	4.60 ^{+0.03} _{-0.02}	0.93 ^{+0.72} _{-0.92}	58508.3 ^{+2.2} _{-2.0}	1.2 ^{+0.06} _{-0.07}	1.65 ^{+0.03} _{-0.03}	-2.1 ^{+0.7} _{-0.7}	1.79 ^{+0.24} _{-0.21}	1.66 ^{+0.16} _{-0.15}
AT2019cho	43.50 ^{+0.01} _{-0.02}	43.98 ^{+0.01} _{-0.01}	4.19 ^{+0.01} _{-0.01}	0.84 ^{+0.21} _{-0.23}	58535.3 ^{+3.0} _{-1.6}	0.8 ^{+0.10} _{-0.11}	1.94 ^{+0.03} _{-0.03}	-1.0 ^{+0.4} _{-0.5}	1.83 ^{+0.25} _{-0.13}	2.19 ^{+0.13} _{-0.16}
AT2019bhf	43.50 ^{+0.05} _{-0.04}	43.91 ^{+0.04} _{-0.05}	4.20 ^{+0.02} _{-0.02}	0.74 ^{+0.15} _{-0.14}	58539.3 ^{+4.4} _{-3.7}	0.6 ^{+0.23} _{-0.35}	1.70 ^{+0.04} _{-0.03}	-1.3 ^{+0.4} _{-0.4}	1.70 ^{+0.23} _{-0.20}	1.96 ^{+0.07} _{-0.09}
AT2019azh	43.33 ^{+0.01} _{-0.01}	44.50 ^{+0.02} _{-0.02}	4.53 ^{+0.01} _{-0.01}	0.98 ^{+0.21} _{-0.19}	58558.6 ^{+1.6} _{-1.5}	1.3 ^{+0.05} _{-0.04}	1.83 ^{+0.01} _{-0.01}	-1.8 ^{+0.2} _{-0.1}	1.87 ^{+0.08} _{-0.08}	1.96 ^{+0.05} _{-0.04}
AT2019dsg	43.22 ^{+0.06} _{-0.05}	44.26 ^{+0.05} _{-0.05}	4.49 ^{+0.04} _{-0.01}	-0.07 ^{+0.14} _{-0.12}	58600.2 ^{+0.6} _{-0.6}	1.2 ^{+0.06} _{-0.12}	1.80 ^{+0.02} _{-0.02}	-1.5 ^{+0.1} _{-0.1}	1.51 ^{+0.11} _{-0.10}	1.59 ^{+0.06} _{-0.06}
AT2019ehz	43.33 ^{+0.01} _{-0.01}	44.03 ^{+0.01} _{-0.02}	4.33 ^{+0.01} _{-0.01}	-0.40 ^{+0.03} _{-0.03}	58611.4 ^{+0.6} _{-0.6}	0.9 ^{+0.03} _{-0.02}	1.67 ^{+0.01} _{-0.01}	-1.8 ^{+0.1} _{-0.1}	1.73 ^{+0.06} _{-0.09}	1.61 ^{+0.04} _{-0.04}
AT2019eve	42.86 ^{+0.02} _{-0.02}	43.14 ^{+0.02} _{-0.03}	4.07 ^{+0.01} _{-0.01}	0.07 ^{+0.08} _{-0.07}	58610.5 ^{+0.5} _{-0.5}	0.1 ^{+0.09} _{-0.07}	2.36 ^{+0.26} _{-0.16}	-0.8 ^{+0.2} _{-1.7}	1.70 ^{+0.87} _{-0.31}	2.25 ^{+0.10} _{-0.10}
AT2019mha	43.30 ^{+0.01} _{-0.01}	44.05 ^{+0.06} _{-0.05}	4.32 ^{+0.03} _{-0.03}	0.36 ^{+0.88} _{-1.07}	58704.0 ^{+0.7} _{-0.8}	1.1 ^{+0.02} _{-0.02}	1.23 ^{+0.03} _{-0.02}	-4.0 ^{+0.7} _{-0.5}	1.63 ^{+0.11} _{-0.12}	1.21 ^{+0.10} _{-0.09}
AT2019meg	43.41 ^{+0.01} _{-0.01}	44.34 ^{+0.03} _{-0.04}	4.43 ^{+0.01} _{-0.01}	1.94 ^{+0.04} _{-0.10}	58696.4 ^{+0.5} _{-0.6}	0.9 ^{+0.02} _{-0.03}	1.72 ^{+0.03} _{-0.02}	-0.5 ^{+0.4} _{-1.1}	2.69 ^{+0.23} _{-0.53}	2.42 ^{+0.14} _{-0.14}
AT2019lwu	43.33 ^{+0.02} _{-0.03}	43.60 ^{+0.03} _{-0.04}	4.09 ^{+0.01} _{-0.01}	0.64 ^{+0.14} _{-0.19}	58690.2 ^{+1.0} _{-0.7}	0.4 ^{+0.17} _{-0.21}	1.68 ^{+0.06} _{-0.05}	-1.5 ^{+0.4} _{-0.5}	1.56 ^{+0.20} _{-0.18}	1.67 ^{+0.09} _{-0.08}
AT2019qiz	42.86 ^{+0.01} _{-0.01}	43.44 ^{+0.01} _{-0.01}	4.28 ^{+0.01} _{-0.01}	-0.17 ^{+0.10} _{-0.09}	58761.4 ^{+0.4} _{-0.4}	0.8 ^{+0.01} _{-0.01}	1.48 ^{+0.01} _{-0.01}	-2.0 ^{+0.1} _{-0.1}	1.40 ^{+0.06} _{-0.06}	1.26 ^{+0.02} _{-0.03}

second source (AT2018hyz), only the g -band light curve is affected. For both sources, sufficient Swift/UVOT photometry is available to obtain a good estimate (uncertainty <0.1 dex) of the light-curve features.

We list the results for the 17 sources with ZTF data in Table 6, and we show the light-curve models in Figure 7. The rest-frame absolute r -band magnitude, and the evolution of the blackbody luminosity, radius, and temperature with time is shown in Figure 8. This study increases the number of TDEs with well characterized prepeak light curves by a factor of 3. We observe a homogeneity in the shape of the radius and temperature evolution. In particular, we point out that most sources show a (modest) increase of the temperature with time.

We find that the typical value of the power-law index of the bolometric luminosity is close to the canonical $p = -5/3 = -1.67$, albeit with large scatter. For the entire sample of 39 TDEs, we find $\bar{p} = -1.56$; restricting the sample to the 31 spectroscopic TDEs yields a similar value of $\bar{p} = -1.57$ with an rms of 0.64. To conclude, the mean power-law index is consistent with $p = -5/3$, but we also find some significant deviations.

5.2. Optical to X-Ray Ratio

In Figure 9, we show a comparison of the 0.3–10 keV X-ray luminosity measured by Swift/XRT to the luminosity of the UV/optical component derived from our light-curve model, for the four new ZTF TDEs with Swift/XRT detections in a single-epoch observation. A fifth ZTF source with X-ray detections was recently presented by Nicholl et al. (2020), obtained after combining multiple XRT epochs. Unlike the UV/optical luminosity, which has a smooth evolution over time and is well described with a single power-law decline post peak, the soft X-ray component shows variability on several timescales (Figure 10). Both large-amplitude flaring on the timescale of just a few days (AT2019ehz) and a dramatic increase in luminosity over a timescale of a few months (AT2019azh) have been observed.

There are only three other TDEs with well-sampled soft X-ray light curves from Swift: ASASSN-14li (Holoien et al. 2014),

ASASSN-15oi (Gezari et al. 2017; Holoien et al. 2018), and AT2018fyk/ASASSN-18ul (Wevers et al. 2019b). While ASASSN-14li showed a soft X-ray flare that followed the general power-law decline of the UV/optical component, with a characteristic ratio of $L_{opt}/L_X \sim 1$ for over a year, the other two TDEs show quite dramatic variability, with a variability and a systematic brightening in the soft X-rays at late times. The first TDE in our ZTF sample, AT2018zr/PS18kh (Holoien et al. 2019b), was detected with a soft X-ray component ($kT \approx 100$ eV) in XMM-Newton observations (van Velzen et al. 2019e), but this component was weak relative to the optical luminosity, $L_{opt}/L_X \sim 100$.

6. Results

At this point, we have extracted the following characteristics from our sample of TDEs: host-galaxy properties (e.g., mass, color, age), three different spectral types of the flare (TDE-H, TDE-He, or TDE-H+He), and ≈ 4 independent light-curve features (blackbody temperature, blackbody radius, rise time-scale, and fade timescale). In this section, we investigate which of these properties are correlated.

6.1. Comparing Spectroscopic TDE Classes

We use the Anderson–Darling (AD²³) statistic to assess whether our three TDE spectral classes show different distributions of light-curve or host properties. The results are summarized in Table 7, and examples of cumulative distributions are shown in Figure 11.

6.1.1. Separation of TDE Photometric Properties with TDE Spectral Class

For the analysis of the light-curve properties, we use only parameters measured with an uncertainty smaller than 0.3 dex.

Comparing the two biggest spectral classes, TDE-H and TDE-H+He, we find a striking difference in the distribution of

²³ An AD comparison of two distributions is similar to the Kolmogorov–Smirnov test, but with increased sensitivity for tails of the distribution.

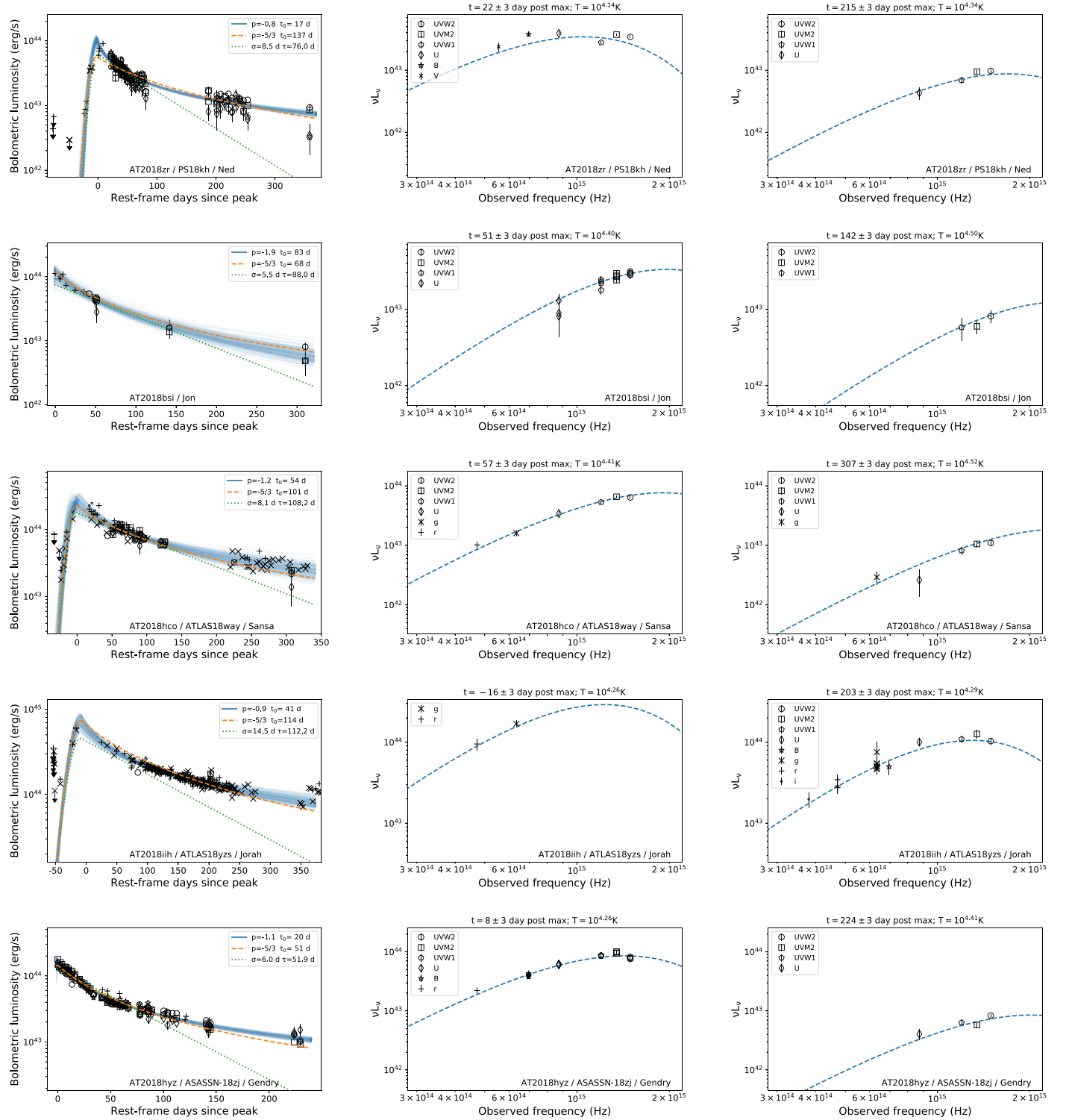


Figure 7. Blackbody light curves and two example SEDs. For each TDE, we show the bolometric light curve, as obtained by fitting Equation (3) to the multiband photometry (solid blue and dashed orange curves; for the latter the power-law index is fixed at $p = -5/3$). The results for an exponential decay are also shown (Equation (2), green dotted line). The dispersion in the power-law model (blue lines) is visualized by drawing samples from the posterior distribution of light curves. For each source, we also show two SEDs, one close to peak and a second one at later times.

blackbody radius. The typical radius of the TDE-H population is a factor of 2 larger than that of the TDE-H+He TDEs. The hypothesis that these two classes are drawn from the same distribution of blackbody radius can be rejected with abundant confidence ($p < 0.001$). The TDE-H and TDE-H+He classes also show a significantly different temperature distribution, the

latter being hotter on average. As on the Rayleigh–Jeans tail the luminosity is given by $L_{\text{RL}} \propto R^2 T$, we also find a significant difference between the distributions of g -band luminosity: the TDE-H class has higher values of L_g .

With only four events, the He-only TDEs are a much smaller sample, yet we still find evidence for differences in rise

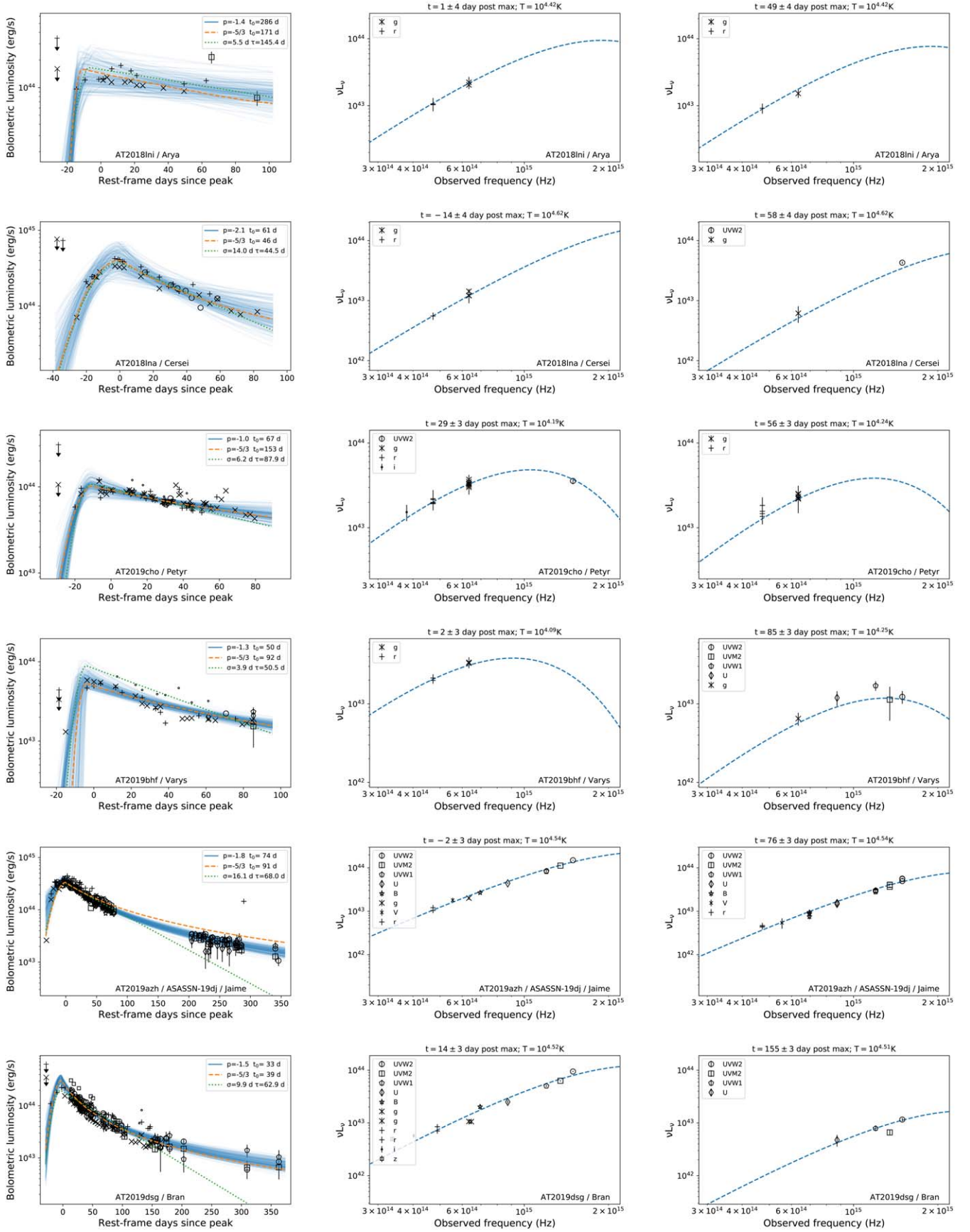


Figure 7. (Continued.)

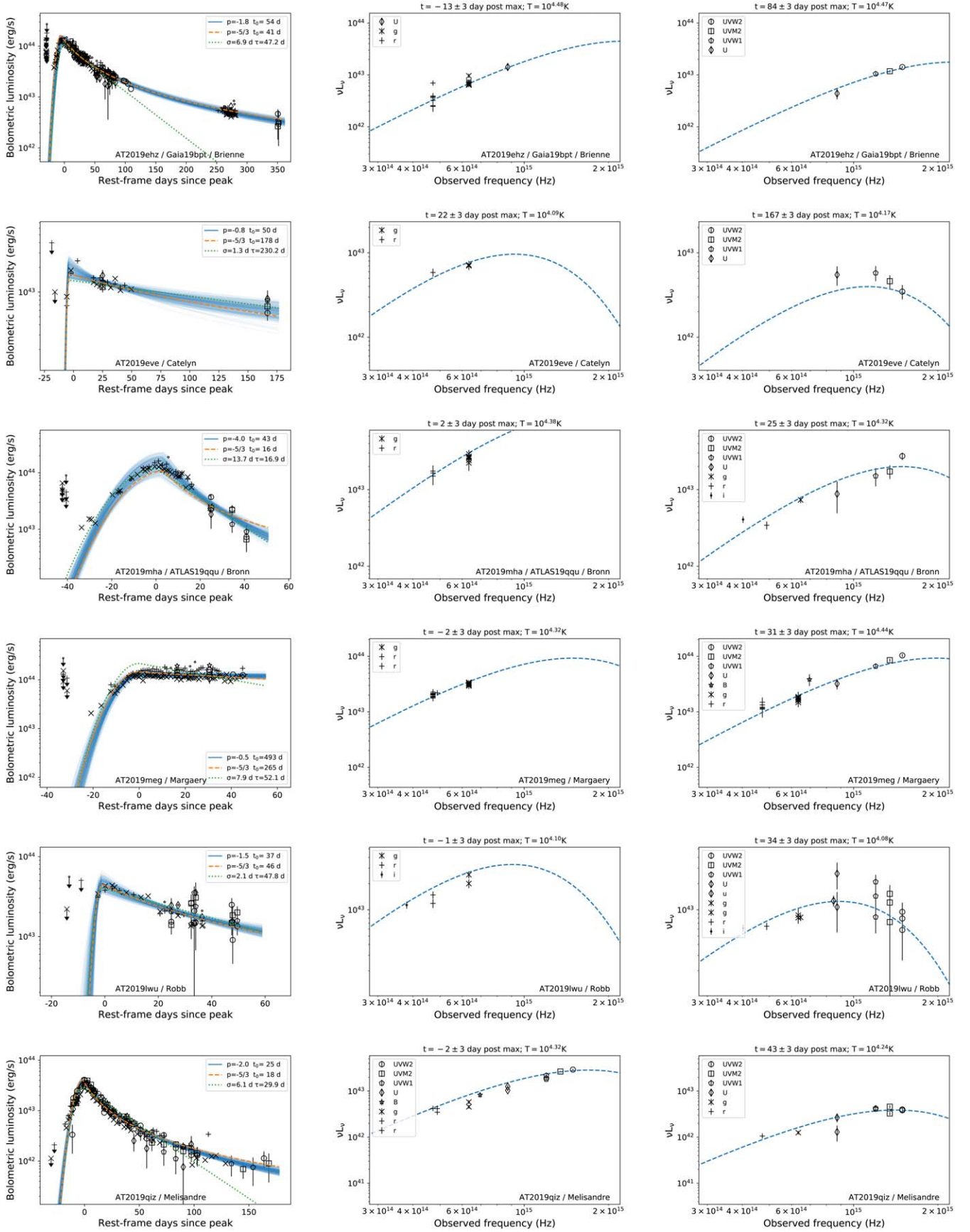


Figure 7. (Continued.)

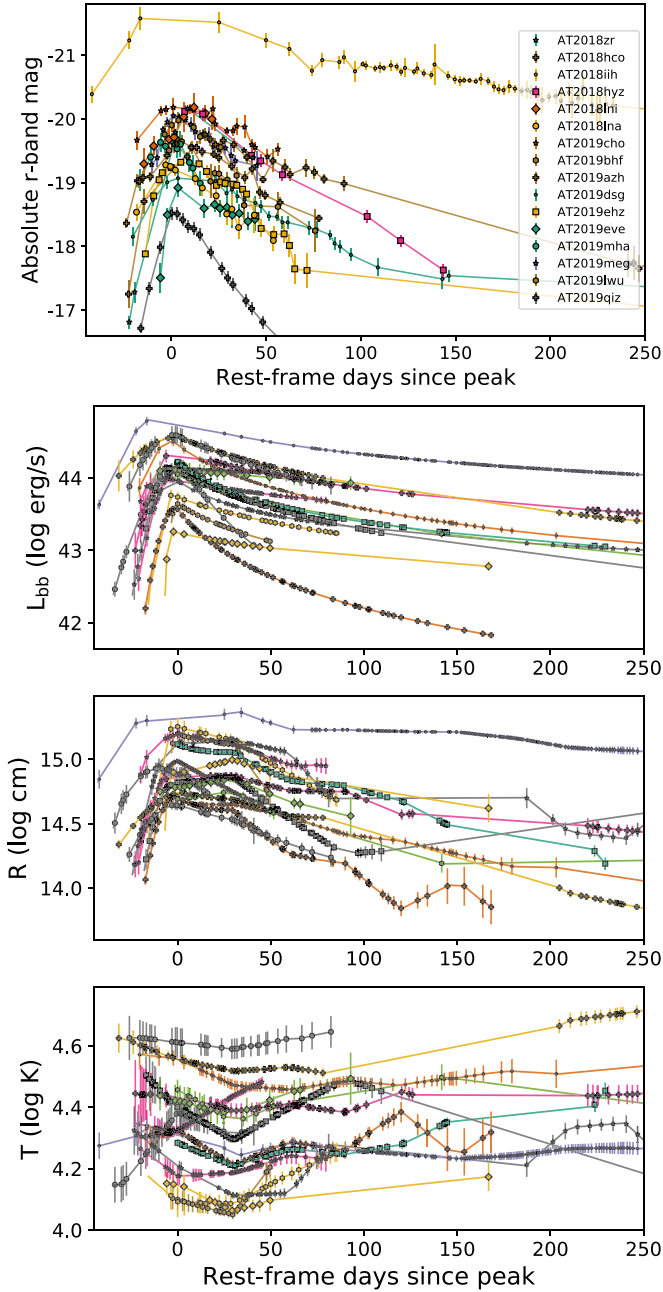


Figure 8. The r -band absolute magnitude, blackbody luminosity, blackbody radius, and rest-frame blackbody temperature for the 17 TDEs in our sample with ZTF and Swift/UVOT observations. We see that all TDEs show a decrease of the blackbody radius after maximum light, and most sources show a small but significant increase of the blackbody temperature.

timescale when compared to the TDE-H class ($p = 0.05$) and g -band luminosity when compared to the TDE-H+He class ($p = 0.025$).

6.1.2. Separation of TDE Host-galaxy Properties with TDE Spectral Class

After noticing that the He-only TDEs appear to have redder host-galaxy $u - r$ colors, we also investigated differences between the TDE spectroscopic classes and their host properties as derived from our population synthesis model. The population parameters are stellar mass, metallicity, age since the peak of star formation, e-folding time of the star formation

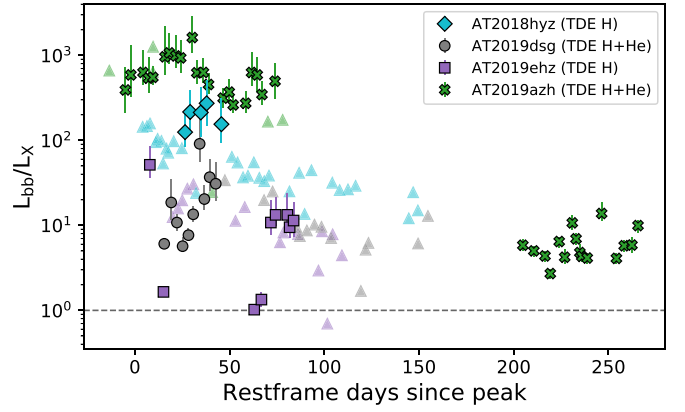


Figure 9. Ratio of the blackbody luminosity derived from the optical/UV light curves to the X-ray luminosity (0.3–10 keV, based on Swift/XRT observations). We call attention to the X-ray flares of AT2019ehz, which reach an X-ray-to-optical ratio close to unity. Triangles indicate 3σ lower limits.

rate (τ_{sfh}), and the dust optical depth. Because we only have five to seven observables (the GALEX FUV and NUV flux or upper limits, plus five bands from SDSS or PS1) the stellar population parameters have large uncertainties and degeneracies. We therefore also consider a principal component analysis (PCA) of these parameters, which should capture the main correlations between the population synthesis parameters (e.g., the age–metallicity degeneracy). We find that the fourth principal component of the galaxy population parameters (PC4 hereafter) yields an apparent separation of the TDE-H and TDE-H+He TDE populations. The weights of PC4 are dominated by the dust parameter and τ_{sfh} .

Motivated by the results of the PCA, we also estimated the combination of population synthesis parameters that yields the maximum separation of the TDE-H and TDE-H+He class. We normalized the five population synthesis parameters by dividing out the median value of each parameter and define

$$C_{\text{max}} = c_1 C_{\text{dust}} + c_2 C_{\text{age}} + c_3 C_{\tau} + c_4 C_Z + c_5 C_{\text{mass}}, \quad (5)$$

with C the normalized population synthesis parameters and c_1 to c_5 a set of free parameters. We used a basin-hopping algorithm to estimate the value of these coefficients that yields the highest AD statistic. We find $c_1 = 1.00$, $c_2 = 0.80$, $c_3 = -0.35$, $c_4 = 0.04$, and $c_5 = -0.43$. In the next section, we will compute the significance of the difference in the C_{max} distribution of TDE-H and TDE-H+He class.

6.2. The “Look Elsewhere” Effect

The look elsewhere effect can cause one to overestimate the significance when multiple trials have been made to search for effects that pass a given threshold for significance. Here we make a correction for this effect on the p values of a single AD test.

If each of the N properties is counted as a trial, and each property is independent, the p value for a single AD test should be increased by $N(1 - p)^{N-1}$. However, our photometric properties are not independent, and we therefore need to use the data directly to estimate the importance of the look elsewhere effect. In our case, $N = 12$, namely 7 parameters of our light-curve model, 5 host-galaxy population synthesis parameters.

To estimate the look elsewhere effect, we repeat the AD test after randomly reordering the spectroscopic TDE labels. On this shuffled data set, we compute the AD statistic for the

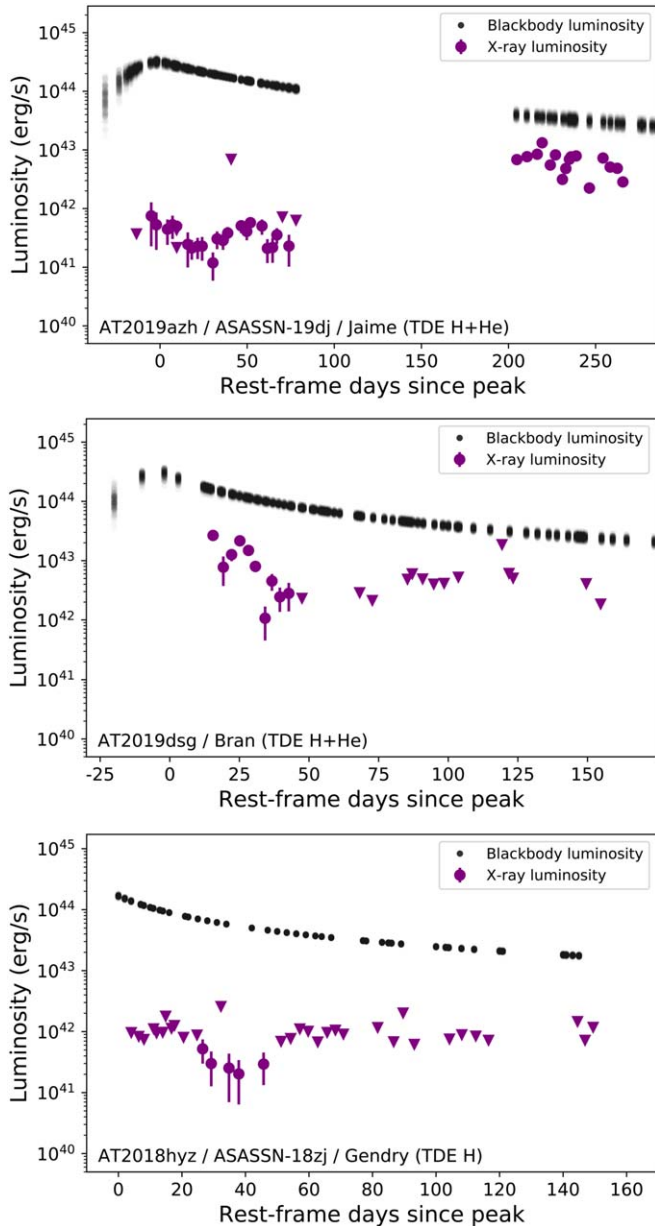


Figure 10. Optical/UV blackbody luminosity (sampled from the posterior distribution) and the observed X-ray 0.3–10 keV luminosity for four TDEs with detections in Swift/XRT single-epoch observations. We see rapid and luminous X-ray flares for AT2019ehz, a steady increase in the X-ray luminosity for AT2019azh, and relatively weak early-time detections for the remaining two sources (AT2019dsg and AT2018hyz). Triangles indicate 3σ upper limits.

parameters that describe the photometric properties of the TDE and its host galaxy. After we repeat this procedure many times, each time shuffling the spectroscopic labels, we obtain a new distribution of the AD statistic of these parameters. We use this trial-corrected distribution to compute the p value of the AD statistic for the parameters listed in Table 7.

As explained in the previous section, the parameter C_{\max} (Equation (5)) is a linear combination of the five host-galaxy population synthesis parameters that yields the largest separation of the TDE-H and TDE-H+He class. To obtain a distribution of the AD statistic that accounts for the trials due to the optimization step, we repeat the computation of C_{\max} each time after shuffling the spectroscopic labels. We find

(Figure 12) that for only 2 in 1000 shuffled data sets is the difference between the TDE-H and TDE-H+He C_{\max} distribution equal to or larger than the observed value (i.e., the hypothesis that C_{\max} values of TDE-H and TDE-H+He class are drawn from the same distribution can be rejected with $p = 0.002$).

6.3. Correlations between TDE Light-curve Properties

In the previous two sections, we presented differences between the TDE spectroscopic classes. We now focus on correlations between TDE light-curve properties, using all 39 TDEs in our sample. When considering the correlation between a pair of parameters, we remove sources with an uncertainty larger than 0.3 dex. The results of a Kendall’s tau test are listed in Table 8. This test only considers the rank of pairs of data points, which is useful because the resulting p value is not disproportionately weighted by large outliers (e.g., ASASSN-15lh). If we instead use a Pearson’s test, which assumes the data follow a normal distribution, we typically find lower (i.e., more significant) p values.

When considering the correlations between a given set of parameters, we need to keep in mind that our data set as a whole shows a large degree of correlation. If all parameters would be uncorrelated, the 36 p values of the correlation test in Table 8 should follow a uniform distribution between 0 and 1, and for a given limit on the significance $p < p_{\text{test}}$, we should find $p_{\text{test}} \times 36$ parameter pairs. Instead, we find that $26/36 = 0.72$ pairs have $p < 0.5$, $16/36 = 0.44$ have $p < 0.1$, and $9/36 = 0.25$ have $p < 0.05$. This means that, similar to what we found in the previous section, spurious correlations due to a larger number of trials are unlikely to be important. However, the large degree of correlation makes it harder to find the causal relation between the parameters.

We find a significant correlation between the blackbody radius and blackbody temperature ($p < 0.001$). The two properties follow the relation expected for a single blackbody spectrum $L_{\text{bb}} \propto R^2 T^4$, with $L_{\text{bb}} \approx 10^{44} \text{ erg s}^{-1}$. This correlation simply confirms that our TDEs are well described by a blackbody spectrum and have a similar luminosity. The scatter around the median luminosity is only 0.3 dex. Because most sources are selected based on optical observations and the bolometric luminosity is largely determined by the temperature estimated from UV follow-up observations, the relatively small scatter cannot be entirely explained by Malmquist bias in our flux-limited sample. As expected, we also find a positive correlation between the blackbody temperature and the blackbody luminosity.

As shown in Figure 13, the rise time of the flare appears to be correlated with the bolometric luminosity. If we consider the ratio of the bolometric luminosity to the blackbody radius, L_{bb}/R , we find a significant correlation with rise time ($p = 0.02$). In Section 7.1, we find that this could be explained by a longer diffusion time at higher densities.

Notably, we find no correlation between the rise timescale and the exponential decay timescale (τ in Equation (2)) or the fallback timescale (t_0 with $p = -5/3$ in Equation (3)).

6.4. Correlations with Host-galaxy Properties

A correlation of TDE light-curve features with host-galaxy properties is anticipated because the black hole mass and the density of the disrupted star should influence the TDE light

Table 7
 p Value of the Anderson–Darling Test Comparing Distributions Separated by TDE Spectral Classes

	H-only versus H+He	H-only versus He-only	H+He versus He-only
Blackbody radius	$p < 0.001$ (13 versus 14)	$p > 0.1$ (13 versus 4)	$p > 0.1$ (14 versus 4)
Blackbody temperature	$p = 0.005$ (13 versus 14)	$p > 0.1$ (13 versus 4)	$p > 0.1$ (14 versus 4)
g -band luminosity	$p < 0.001$ (13 versus 14)	$p > 0.1$ (13 versus 4)	$p = 0.025$ (14 versus 4)
Blackbody luminosity	$p > 0.1$ (13 versus 14)	$p > 0.1$ (13 versus 4)	$p > 0.1$ (14 versus 4)
Rise e-folding time	$p > 0.1$ (9 versus 9)	$p = 0.049$ (9 versus 3)	$p > 0.1$ (9 versus 3)
Decay e-folding time	$p > 0.1$ (11 versus 14)	$p > 0.1$ (11 versus 4)	$p > 0.1$ (14 versus 4)
Fallback time	$p > 0.1$ (11 versus 14)	$p > 0.1$ (11 versus 3)	$p > 0.1$ (14 versus 3)
Power-law index	$p = 0.078$ (8 versus 8)	$p > 0.1$ (8 versus 3)	$p > 0.1$ (8 versus 3)
Redshift	$p > 0.1$ (13 versus 14)	$p > 0.1$ (13 versus 4)	$p > 0.1$ (14 versus 4)
Host mass	$p > 0.1$ (13 versus 14)	$p > 0.1$ (13 versus 4)	$p > 0.1$ (14 versus 4)
Host rest-frame $u - r$	$p > 0.1$ (13 versus 14)	$p > 0.1$ (13 versus 4)	$p > 0.1$ (14 versus 4)
Time since peak SFR	$p > 0.1$ (13 versus 14)	$p > 0.1$ (13 versus 4)	$p > 0.1$ (14 versus 4)
SFH τ	$p > 0.1$ (13 versus 14)	$p > 0.1$ (13 versus 4)	$p > 0.1$ (14 versus 4)
Host metallicity	$p > 0.1$ (13 versus 14)	$p > 0.1$ (13 versus 4)	$p > 0.1$ (14 versus 4)
Host dust $E(B - V)$	$p > 0.1$ (13 versus 14)	$p > 0.1$ (13 versus 4)	$p > 0.1$ (14 versus 4)
Host population synthesis PC1	$p > 0.1$ (13 versus 14)	$p > 0.1$ (13 versus 4)	$p > 0.1$ (14 versus 4)
Host population synthesis PC2	$p > 0.1$ (13 versus 14)	$p > 0.1$ (13 versus 4)	$p > 0.1$ (14 versus 4)
Host population synthesis PC3	$p > 0.1$ (13 versus 14)	$p > 0.1$ (13 versus 4)	$p > 0.1$ (14 versus 4)
Host population synthesis PC4	$p > 0.1$ (13 versus 14)	$p > 0.1$ (13 versus 4)	$p > 0.1$ (14 versus 4)
Host population synthesis C_{\max}	$p = 0.002$ (13 versus 14)	$p > 0.1$ (13 versus 4)	$p > 0.1$ (14 versus 4)

Note. Parameter distributions that show a significant difference ($p < 0.05$) are highlighted in green. The p values have been corrected for the number of trials (see Section 6.1). The number of sources in each class are listed in the brackets.

curve. Black hole mass estimates from the stellar velocity dispersion are not (yet) available for most TDEs in our sample, and we therefore use the total host-galaxy mass obtained from the host photometry (Section 3) as a proxy for black hole mass.

In Figure 14, we show a number of TDE properties as a function of total galaxy mass, and in Table 8, we list the significance. Using a Kendall’s tau test, a significant correlation is found for the monochromatic decay timescale measured during the first 100 days (τ , $p = 0.005$). The host-galaxy mass also appears to be correlated with the fallback timescale, but the scatter is larger the correlation is weaker.

We also investigated correlations between the photometric TDE properties and the combination of host-galaxy properties that separates the TDE-H and TDE-H+He class, C_{\max} (Equation (5)). Using all 39 TDEs, we find a significant correlation between C_{\max} and the three photometric properties: rise time ($p = 0.03$), blackbody temperature ($p = 0.03$), and radius ($p = 0.01$); see Table 7. We also find an correlation ($p = 0.01$) between the second host-galaxy PCA component, which is dominated by the mass and metallicity parameters, and the TDE rise time. This is interesting because the correlation between rise time and stellar mass alone is not significant (see Figure 14).

7. Discussion

The main challenge for a TDE emission model is to turn the fallback rate of the stellar debris, which can be calculated or simulated with reasonable accuracy (e.g., Lodato et al. 2009; Guillochon & Ramirez-Ruiz 2013), into an electromagnetic output. As shown in Figure 7, when TDEs are observed for longer than ~ 100 days, a power-law decay is required to explain the observed light curves. The median power-law index of the 39 TDEs in our sample is $p = -1.6$, which is close to the value expected for the full disruption of a star, $p = -5/3$. This result has been noticed in earlier, smaller samples of TDEs

(e.g., Gezari et al. 2009; Piran et al. 2015; Hung et al. 2017) and is an important motivation to construct TDE emission models that couple the (postpeak) bolometric luminosity to the fallback rate (Guillochon et al. 2014; Piran et al. 2015; Krolik et al. 2016; Mockler et al. 2019; Bonnerot & Lu 2020).

In this work, we find a correlation between the decay timescale and total galaxy stellar mass, which is consistent with previously reported correlations between decay time and black hole mass (Blagorodnova et al. 2017; Wevers et al. 2017). This supports the idea that the fallback timescale can be measured from the postpeak TDE light curve. Indeed, Mockler et al. (2019) find that the light curves of an earlier sample of TDEs (most without prepeak detections) are consistent with “prompt” emission (i.e., light curves that directly trace the theoretical fallback rate).

Our new sample contains 21 spectroscopic TDEs with well-measured rise times, providing a new regime to test models for the emission mechanism. We find no correlation between the rise timescale of the light curve and the decay timescale nor any significant correlation of the rise time with total galaxy mass. In the next section, we discuss how the lack of correlation between rise time and galaxy stellar mass (acting as a proxy for black hole mass) is in fact expected for two separate theoretical scenarios of optical emission from TDE.

7.1. Photon Advection and Diffusion

In the model by Metzger & Stone (2016), the optical radiation will be advected through an outflowing wind until it reaches the trapping radius (R_{tr}), the location at which the radiative diffusion time through the remaining debris is shorter than the outflow expansion time. It is useful to introduce the trapping time t_{tr} , which is the time photons are losing a significant amount of energy from being trapped in the wind and adiabatically transferring energy to the outflow. For low-mass black holes, $M_{\text{BH}} \lesssim 7 \times 10^6 M_{\odot}$, Metzger & Stone (2016)

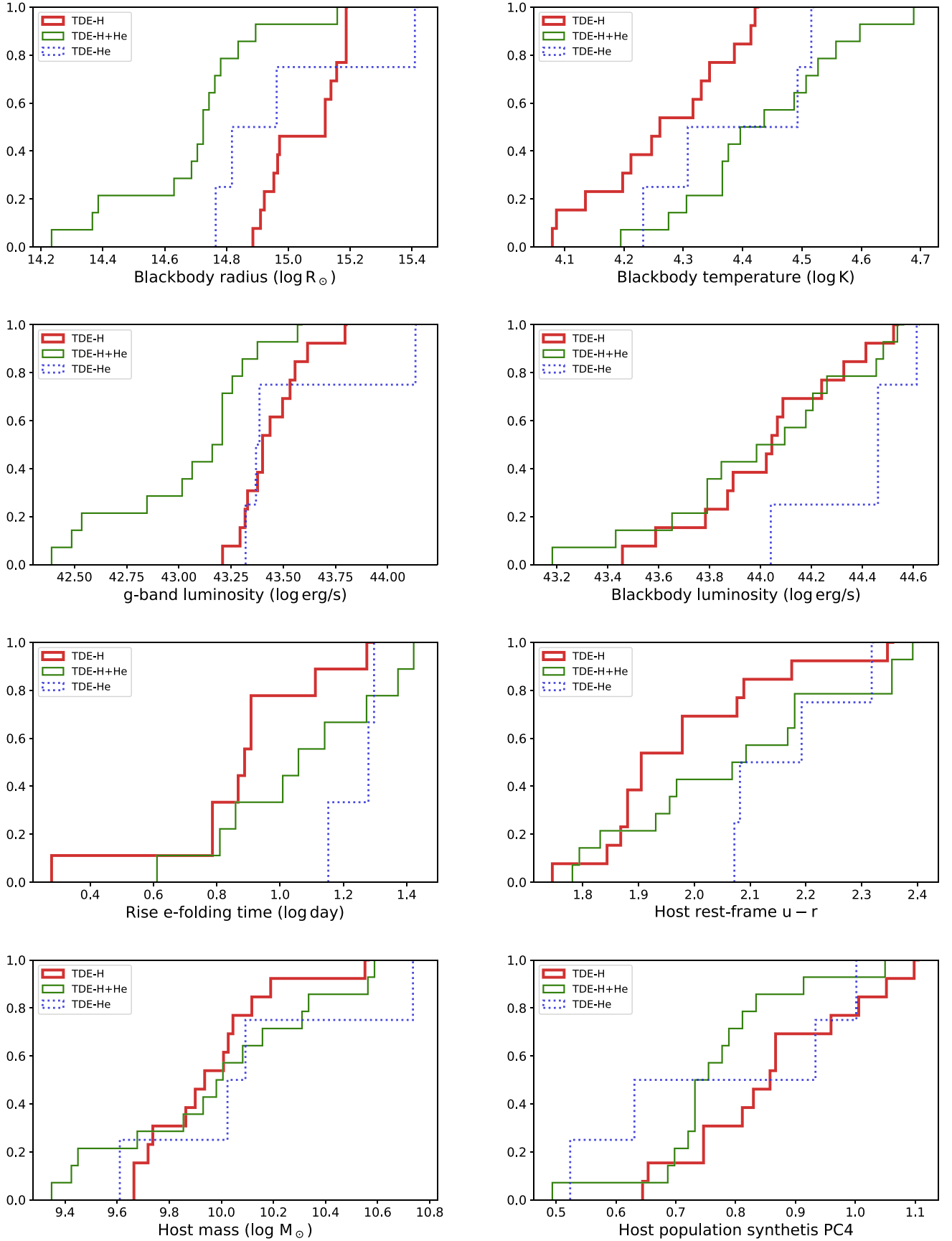


Figure 11. Cumulative distribution of light-curve and host-galaxy properties for different TDE spectroscopic classes. The TDE-H and TDE-H+He spectroscopic classes show a significantly different distribution of blackbody radius and temperature. The He-only TDEs appear to separate from the other two groups by their higher luminosity and longer rise time.

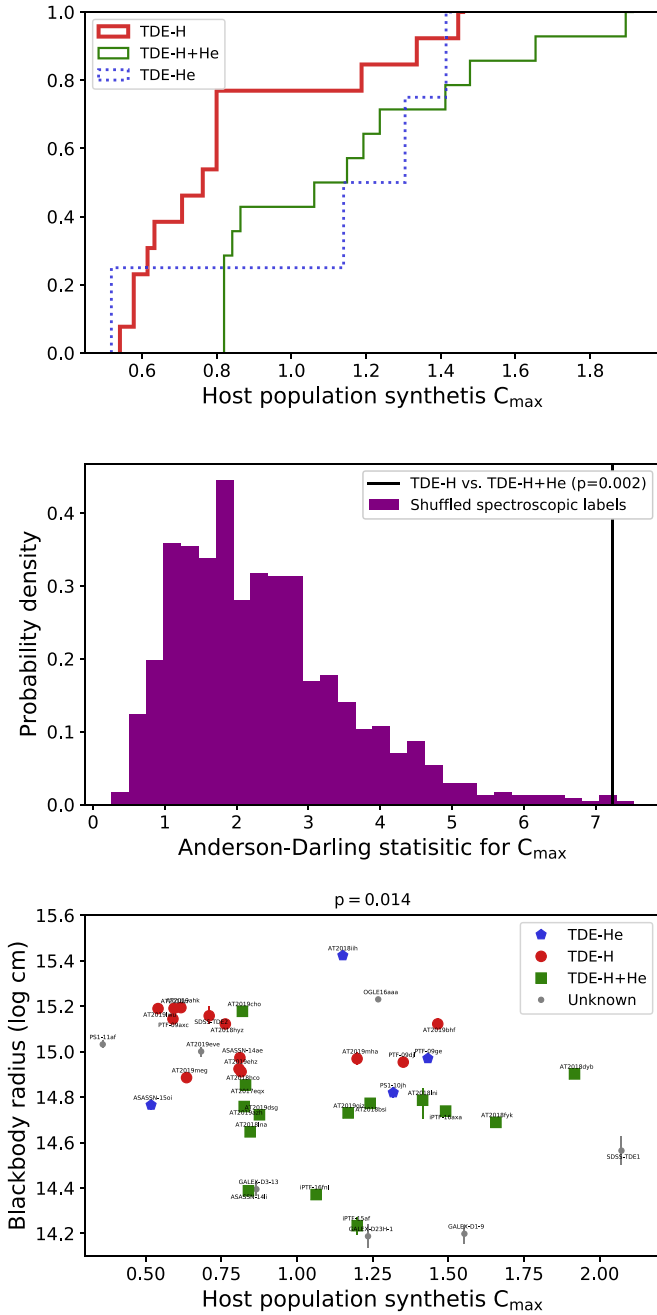


Figure 12. The parameter C_{\max} is a superposition host-galaxy population synthesis parameters that yields the maximum separation of the TDE-H and TDE-H+He class, as measured by the AD statistic. The cumulative distribution of this parameter is shown in the top panel. The middle panel illustrates the significance of the difference between the TDE-H and TDE-H+He class. If we randomly redistribute the TDE spectroscopic labels, only in 2 out of 1000 cases do we find an equally strong separation. In the bottom panel we show C_{\max} vs. the blackbody radius at the peak of the optical/UV light curve. The p value for Kendall's tau test ($p = 0.01$) is measured including the sources without a spectroscopic label.

find that $t_{\text{tr}} > t_{\text{fb}}$, and thus adiabatic losses suppress and delay the peak of the TDE light curve. In this case, the predicted correlation between the peak luminosity L_{pk} and M_{BH} is extremely weak, $L_{\text{pk}} \propto M_{\text{BH}}^{0.06}$. This results from a cancellation of effects: for larger M_{BH} , the longer t_{fb} causes the accretion rate powering the outflow to be lower, but the photons are also less trapped in the outflow and so retain more of their energy.

This weak correlation between L_{pk} and M_{BH} also manifests as a weak correlation between t_{pk} and M_{BH} , again for these lower black hole masses. At higher black hole mass, the relations $L_{\text{pk}} \propto M_{\text{BH}}^{-1/2}$ and $t_{\text{pk}} \propto M_{\text{BH}}^{1/2}$, as expected from the mass fallback relations, should reappear.

Alternatively, in the description of Piran et al. (2015), there is no outflow, and the size of the UV/optical emitting region is tied to the apocenter of the most bound stellar debris. For sufficiently low-mass black holes, the diffusion time t_{diff} for photons to escape the shock-heated debris will provide a timescale that must be convolved with the shock-heating rate set by t_{fb} to produce the final light curve. For sufficiently low black hole mass, t_{diff} may become long enough that the black hole mass dependence inherent in t_{fb} may be washed out by the diffusion time, which is itself more strongly correlated with the mass and structure of the disrupted star than with the black hole mass. For higher-mass black holes, as was the case for Metzger & Stone (2016), these radiative transfer effects should diminish in importance; we again expect the mass fallback relations to dictate the shape of the light curve.

To conclude, the lack of significant correlations between light-curve rise time and host-galaxy stellar mass in our sample of TDEs could be explained by photon advection or diffusion, because these will interfere with seeing an unmitigated signal from the mass fallback rate.

The diffusion timescale for electron scattering scales as $t_{\text{diff}} \propto \rho R^2$ (e.g., Metzger & Stone 2017). For a spherical distribution of mass within the photosphere radius R , we find $t_{\text{diff}} \propto M/R$. If the peak blackbody luminosity (L_{bb}) is proportional to this mass, we obtain $t_{\text{diff}} \propto L_{\text{bb}}/R$. This scaling of the diffusion time and the ratio of blackbody luminosity and radius could explain the observed correlation between L_{bb}/R and the rise timescale (Figure 13).

7.2. Event Rate and Stellar Mass

An important property of the TDE-H+He class is their low optical luminosity. Because they are detected in numbers equal to the H-only class, this low luminosity implies a higher intrinsic rate. To estimate the magnitude of this effect, we use the empirical g-band luminosity function of TDEs (van Velzen 2018) to assign a rate to each TDE based on its observed g-band luminosity. In Figure 15, we show the result as a function of blackbody radius; we find a steep dependence on radius, $dN/dR \propto R^{-3}$.

If the optical/UV blackbody radius would be proportional to the mass of the star, we obtain a potential explanation for steep decline of the event rate with blackbody radius (Figure 15). Such a scaling is in fact expected if the photosphere is proportional to the self-intersection radius of stream. In Figure 16, we show the radius of an accretion disk created from energy dissipated at the self-intersection radius as a function of black hole mass and stellar mass, obtained using the formalism²⁴ of Dai et al. (2015) and the mass-radius relations for high-/low-mass main-sequence stars from Kippenhahn & Weigert (1990). If we assume that the blackbody photospheric

²⁴ Dai et al. (2015) provide formulas for the location of the stellar debris intersection and estimates for the resulting rate of energy dissipation at the intersection shock, by using an impulse approximation for general relativistic precession, to leading post-Newtonian order. In this way, they derive an approximate formula for the semimajor axis of the elliptical disk that forms immediately following the stream intersection, which depends on the mass of the star, the mass of the black hole, and the dimensionless impact parameter β .

Table 8
Kendall’s tau p -Value Comparing Photometric and Host-galaxy Properties

	R	T	L_{bb}	Rise	Decay	z	Host Mass	Host $u - r$	Host C_{max}
R	...	<0.001(39)	>0.1 (39)	>0.1 (26)	>0.1 (36)	>0.1 (39)	>0.1 (39)	>0.1 (39)	0.014(39)
T	0.017(39)	0.047(26)	>0.1 (36)	>0.1 (39)	>0.1 (39)	>0.1 (39)	0.025(39)
L_{bb}	0.086(26)	>0.1 (36)	0.051(39)	0.093(39)	>0.1 (39)	>0.1 (39)
Rise	>0.1 (23)	>0.1 (26)	>0.1 (26)	>0.1 (26)	0.030(26)
Decay	0.021(36)	0.005(36)	>0.1 (36)	>0.1 (36)
z	0.011(39)	>0.1 (39)	>0.1 (39)
Host mass	<0.001(39)	0.061(39)
Host $u - r$	0.008(39)
Host C_{max}

Note. Parameter sets that show a significant correlation ($p < 0.05$) are highlighted in green. The number of sources in each set is listed in brackets. The parameter C_{max} is a linear combination of the host-galaxy population synthesis parameters that yields a maximum separation of the TDE-H and TDE-H+He class.

radius R is proportional to the disk size, from Figure 16 we see that, all else being equal, lower mass stars are associated with smaller values of R ; at $M_{\text{BH}} = 10^{6.5} M_{\odot}$, $\log(R) \approx 0.8 \log(M_*)$. Using this result, we find that smaller blackbody radii imply higher blackbody temperatures, consistent with the observed scaling $T \propto R^{-1/2}$ (Figure 6). On the Rayleigh–Jeans tail, we have $L_{\nu} \propto L_{\text{bb}}^{1/4} R^2 T \propto L_{\text{bb}}^{1/4} R^{3/2} \propto L_{\text{bb}}^{1/4} M_*^{1.2}$. For a typical initial mass function ($dN/dM_* \propto M_*^{-2.3}$), the higher number density of low-mass stars thus provides a simple explanation for the steep decrease of the event rate with blackbody radius ($dN/dR \propto R^{-3}$, Figure 15).

The greatest distinction between the TDE-H and TDE-H+He classes is that the latter is characterized by smaller radii (e.g., Figures 13 or 11). Here we recall that almost all sources in the TDE-H+He class show evidence for Bowen lines and that this fluorescence mechanism requires both a high flux of EUV photons and a high gas density. Because the observed blackbody luminosity is similar for the TDE-H+He and TDE-H class, we may infer that the small radii of the TDE-H+He class can be explained by the high-density conditions that enable their fluorescent lines. If we again assume that the optical/UV blackbody radius is related to the stream self-intersection radius (Figure 16), the density within a spherical emission region ($\rho \sim M_*/R^3$) will decrease with stellar mass. It thus appears that we can explain both higher density within the photosphere and the higher rate of the TDE-H+He class with the disruption of lower mass stars.

The TDE-He class presents an interesting case to test the idea that the photosphere radius is set by properties of the disrupted star. The He-only class has the longest rise times and highest luminosities, yet relatively large photosphere radii (Figure 13). We either need a high-mass star that is relatively dense, or a high-mass star and a high impact parameter. Both of these scenarios would explain why this spectroscopic class is rare. The lack of H emission would then be a signature either of the lack of hydrogen in a dense He star (Gezari et al. 2012) or the radiative transfer effects in a dense reprocessing region (Guillochon et al. 2014; Roth et al. 2016).

7.3. Correlations with Host-galaxy Stellar Population Parameters

The observation that the TDE-H and TDE-H+He classes show significant differences in the distribution of stellar population parameters (Table 7) could in principle be used to shed light on which stellar properties (e.g., density, composition, or impact parameter) influence the TDE light curve and

spectrum. Unfortunately, the interpretation of the population parameters is not straightforward.

The superposition of the host-galaxy stellar population synthesis parameters that yields the largest separation of the TDE-H and TDE-H+He class is mainly driven by the dust optical depth (C_{dust}) plus the age of the stellar population (C_{age}), minus e-folding time of the star formation (C_{τ}), such that the TDE-H+He class has higher values of $C_{\text{dust}} + C_{\text{age}} - C_{\tau}$. Yet the Bowen TDEs also have the highest blackbody temperatures, implying that they are not systematically affected by dust in their host galaxies. We therefore expect that the dust parameter absorbs the imperfections of our simple single-age stellar population model. At this point, we can speculate that the age of the stellar population is the underlying cause for the difference between the TDE spectroscopic classes. But the correct path forward is to improve our inference of the stellar population by including additional information, such as the WISE photometry and the absorption-line diagnostics (e.g., French et al. 2017). This will be the subject of future work.

7.4. Surprises from the Optical/X-Ray Ratio

Most models that use reprocessing of photons from close to the black hole to explain the observed optical emission of TDEs predict that at some point, the reprocessing layer becomes transparent to X-rays. In the outflow model by Metzger & Stone (2017), the inner wind becomes transparent to X-ray radiation once it is fully ionized by emission from the inner accretion disk, which happens at $t_{\text{ion}} \approx 0.8 t_{\text{fb}} (M_{\text{BH}}/10^6 M_{\odot})^{-0.8} (M_*/M_{\odot})^{0.4}$. At this point, the reprocessing efficiency decreases, and one would expect an increase of the ratio of the X-ray to optical/UV luminosity (L_X/L_{bb}). Alternatively, if our view of the inner accretion disk is unobscured and the optical emission originates from the stream intersection point (Piran et al. 2015), an increase of the X-ray importance is evidence for delayed accretion onto the black hole (as seen in the simulations of Shiokawa et al. 2015).

Because the inner accretion disk itself should also produce optical/UV emission (Cannizzo et al. 1990; Strubbe & Quataert 2009; Lodato & Rossi 2011), the optical luminosity is unlikely to completely vanish when the reprocessing layer is fully ionized. Indeed, late-time observations of TDEs (\sim few years after peak) show a near-constant luminosity that is consistent with an accretion disk (van Velzen et al. 2019c; Jonker et al. 2020; Mummery & Balbus 2020).

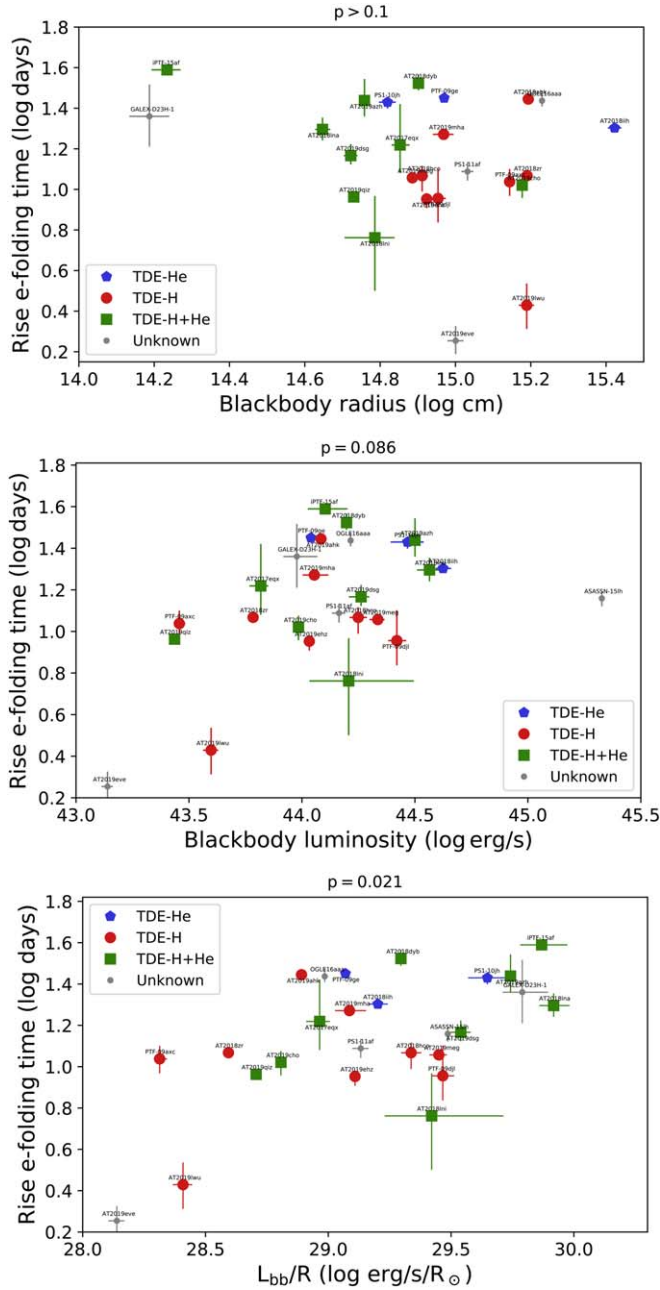


Figure 13. Rise time vs. blackbody radius (R), blackbody luminosity (L_{bb}), and L_{bb}/R . We see that sources with smaller blackbody radii have the longest rise times, and the TDEs with only helium emission lines in their optical spectra (TDE-He) have significantly longer rise times compared to the rest of the population. While the blackbody radius and luminosity are not correlated with each other (Figure 6), the rise time appears to be correlated with both of these light-curve properties (top and middle panels). The strongest correlation is found between the rise time and the ratio of the luminosity and radius (lower panel). These results can be explained if the rise time is proportional to the density inside the photosphere (Section 7.1).

The dramatic brightening of AT2019azh in the soft X-rays 7 months after peak is similar to the behavior of TDE ASASSN-15oi (Liu et al. 2019), which was interpreted by Gezari et al. (2017) as a result of delayed accretion. However, the faint flux in the soft X-rays could also be explained by a suppression from adiabatic losses due to electron scattering (Dai et al. 2018). In contrast to the preferential suppression of soft X-rays associated with atomic absorption, these adiabatic losses leave

a subtler imprint on the spectral slope of the attenuated X-ray spectrum, potentially consistent with the lack of strong evolution in the X-ray spectra when L_{bb}/L_X decreases.

One TDE in our sample (AT2019ehz) shows a remarkable, and hitherto unseen, evolution of L_{bb}/L_X . We observe three X-ray flares during the first months of post-peak observation (Figure 9), increasing its X-ray luminosity by almost two orders of magnitude to $L_X \approx 5 \times 10^{44} \text{ erg s}^{-1}$ on a timescale of days. The peak X-ray luminosity of the flares is just below the optical/UV blackbody luminosity measured at the same time (Figure 10). If stream collisions are the main power source of early-time optical TDE emission (i.e., accretion is energetically unimportant), the X-ray flares of AT2019ehz could in principle be explained by parcels of gas that are deflected toward the black hole from the stream collision site. However, the short timescale of the observed flare implies these discrete parcels would have to be aimed very precisely, which is not expected; the simulation by Shiohara et al. (2015) does show fluctuations in the mass accretion rate, but these occur on a timescale that is longer than the fallback time. We also note that it would be a coincidence that for each of the three flares, the X-rays from the gas deflected by shocks reach $L_{\text{bb}}/L_X \sim 1$. On the other hand, an equal amount of intrinsic accretion luminosity and observed optical/UV luminosity is a generic feature of a reprocessing layer with a high covering factor. In this scenario, the X-ray flares are not due to an increase of the accretion rate but to a decrease of the optical depth to our line of sight of the compact X-ray emitting region.

Obtaining a few brief glimpses of the central soft X-ray emission would be possible for a reprocessing region that is moderately patchy. Because the size of this accretion disk is ~ 100 times smaller than the optical photosphere, our hypothetical patchy reprocessing layer can have many small “gaps” that provide a view of the disk while the reprocessing efficiency remains high. Adapting the equation for the orbital timescale of a gas cloud at r_{orb} from LaMassa et al. (2015), we get a crossing timescale of

$$t_{\text{cross}} = 0.22 \left[\frac{r_{\text{orb}}}{\text{lt-day}} \right]^{3/2} \left(\frac{M_{\text{BH}}}{10^7 M_{\odot}} \right)^{-1/2} \arcsin \left[\frac{r_{\text{src}}}{r_{\text{orb}}} \right] \text{yr}. \quad (6)$$

For a small gap, the distance of the optical photosphere of $10^{14.5} \text{ cm} = 0.1 \text{ lt-day}$, we get a crossing time of 2.5 days, in agreement with the duration of the soft X-ray flares.

8. Conclusions

1. We present 17 TDEs with light curves from ZTF, selected based on the photometric properties of nuclear ZTF transients (Figure 1).
2. Galaxies in the green valley are overrepresented in our ZTF sample by a factor of ≈ 5 (Figure 3).
3. Based on the ZTF and Swift/UVOT photometry, we find that most of the TDEs in our sample show an increase of the temperature with time (Figure 8, Table 6).
4. After including spectroscopic TDE from the literature, we obtain 31 sources that we classify into three classes: TDE-H, TDE-He, and TDE-H+He (Section 2.4). Almost all sources in the TDE-H+He class show evidence for Bowen fluorescence lines.
5. We find significant differences between the photometric properties of the TDEs in each spectroscopic class

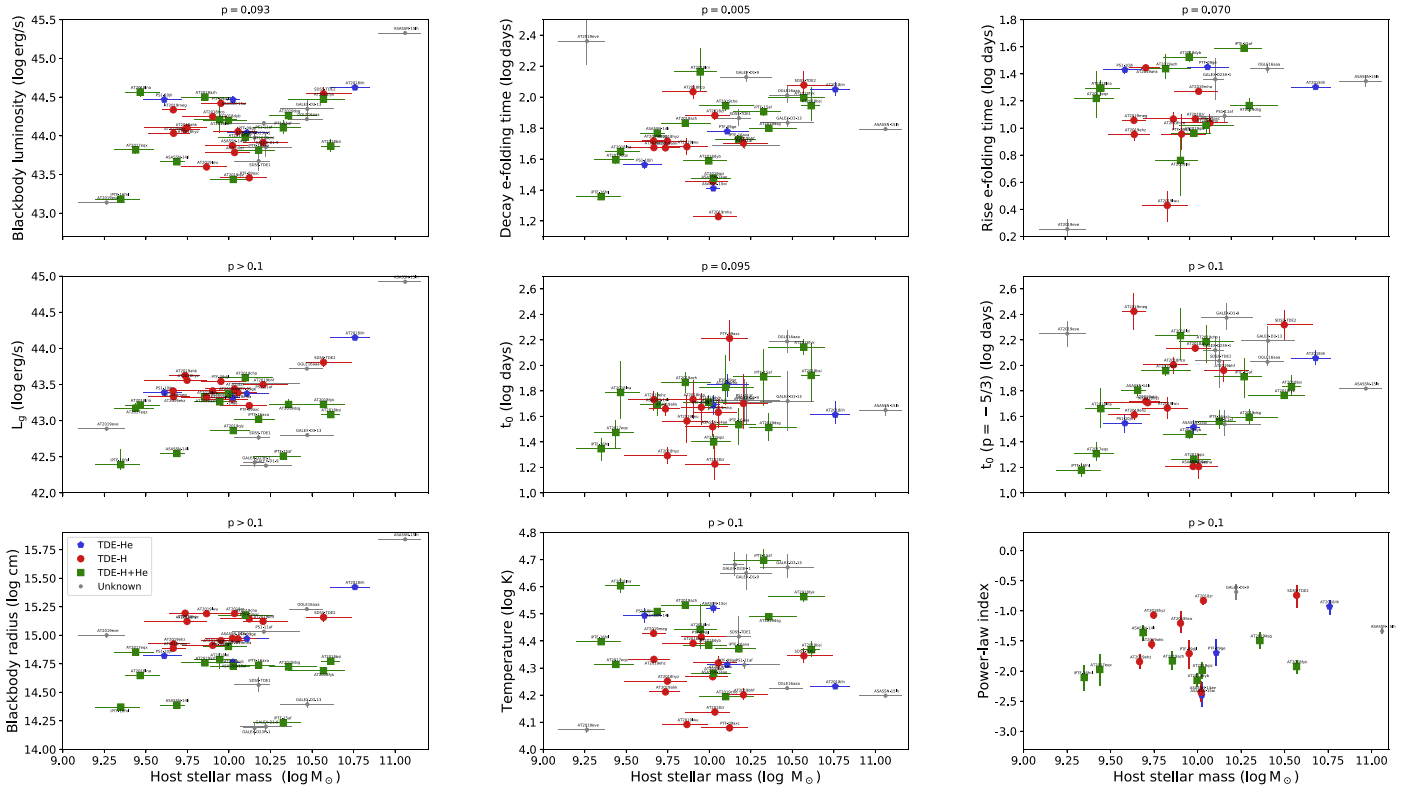


Figure 14. TDE light-curve properties vs. the total stellar mass obtained from the host photometry. The marker symbol and color indicate the TDE spectroscopic class (the legend is printed in the first panel of the last row). The p value of a Kendall's tau test for correlation between the two properties can read at the top of each panel. We find a significant correlation between host mass and the decay timescale (τ ; Equation (2)).

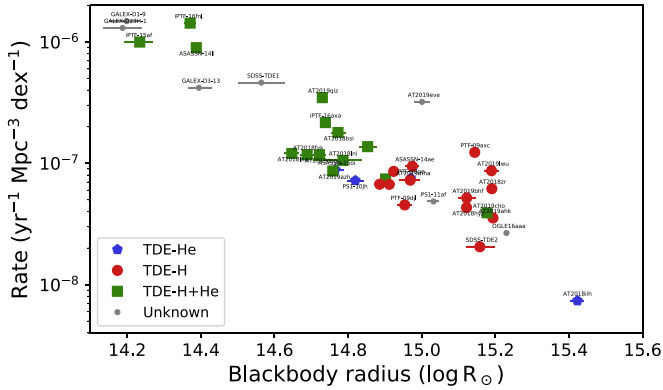


Figure 15. The approximate event rate as a function of blackbody radius at peak. For each TDE, we plot the rate corresponding to its g -band luminosity, using the empirical luminosity function of van Velzen (2018). We see a strong decrease of the event rate with blackbody radius (roughly scaling as $dN/dR \propto R^{-3}$). If the photosphere is proportional to the mass of the disrupted star (Section 7.2), this trend can be explained by the slope of the initial mass function of stars (i.e., low-mass stars, and thus small radii, are more common).

(Table 7). Most notably, the TDE-H+He class has smaller radii and lower rest-frame g -band luminosities (Figures 6 and 11).

6. Below an optical/UV photosphere radius of $10^{14.8}$ cm, all TDEs are spectroscopically classified as H+He.
7. We find statistically significant differences in the host-galaxy population synthesis properties (dust, SFH, metallicity, mass) for the TDE-H and TDE-H+He class. Using the entire sample of photometric+spectroscopic TDEs, we also find significant correlations between stellar population

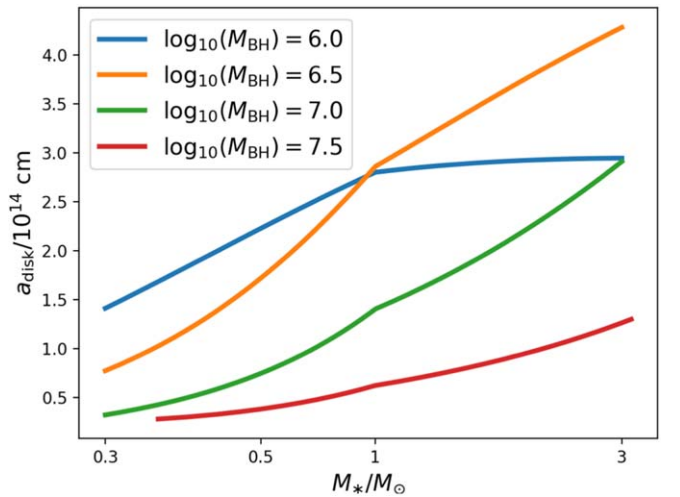


Figure 16. The estimated size of the disk following dissipation at the stream intersection shock, computed following Dai et al. (2015). We show this radius as a function of stellar mass and black hole mass, for stellar orbits with a pericenter equal to the tidal radius ($\beta = 1$, which are expected to be the most common). We see that the disk size increases with stellar mass. Because low-mass stars are more numerous and thus get disrupted more often, this connection between stellar mass and disk radius could explain the observed decrease of the disruption rate as a function of blackbody radius (Figure 15).

- parameters and the TDE blackbody radius, temperature, and rise timescale (Section 6.4).
8. We find a correlation between host-galaxy total mass and the decay timescale of the light curve (Figure 14 and Table 8), suggesting that the shape of the postpeak light

curve is related to the fallback timescales and thus contains information about the mass of the black hole that disrupted the star.

9. We identified a significant correlation between the rise timescale and L_{bb}/R (Figure 13). The rise time is neither correlated with host-galaxy mass nor with the decay timescale. These results can be explained by photon diffusion, which delays the time to maximum light (Section 7.1).
10. Four sources are detected in the Swift/XRT observations. In one case (AT2019ehz), we observed three rapid X-ray flares (Figures 9 and 10). The peak luminosity of the X-ray flares approaches the optical/UV blackbody luminosity measured at the time of the flare. These similar luminosities at different wavelengths can be explained if the optical light is due to reprocessing of accretion power in a region with a high covering factor and some gaps that allow the central engine to be briefly visible.

We thank the referee for the useful and constructive comments.

Based on observations obtained with the Samuel Oschin Telescope 48 inch and the 60 inch Telescope at the Palomar Observatory as part of the Zwicky Transient Facility project. ZTF is supported by the National Science Foundation under grant No. AST-1440341 and a collaboration including Caltech, IPAC, the Weizmann Institute for Science, the Oskar Klein Center at Stockholm University, the University of Maryland, the University of Washington, Deutsches Elektronen-Synchrotron and Humboldt University, Los Alamos National Laboratories, the TANGO Consortium of Taiwan, the University of Wisconsin at Milwaukee, and Lawrence Berkeley National Laboratories. Operations are conducted by COO, IPAC, and UW. SED Machine is based upon work supported by the National Science Foundation under grant No. 1106171.

We thank the Swift team, including the Observation Duty Scientists, and the science planners for promptly approving and executing our Swift observations. We also acknowledge the use of public data from the Swift data archive. This work made use of data supplied by the UK Swift Science Data Centre at the University of Leicester.

These results made use of the Discovery Channel Telescope at Lowell Observatory. Lowell is a private, nonprofit institution dedicated to astrophysical research and public appreciation of astronomy and operates the DCT in partnership with Boston University, the University of Maryland, the University of Toledo, Northern Arizona University and Yale University. The upgrade of the De Veny optical spectrograph has been funded by a generous grant from John and Ginger Giovale.

The W. M. Keck Observatory is operated as a scientific partnership among the California Institute of Technology, the University of California, and NASA; the Observatory was made possible by the generous financial support of the W. M. Keck Foundation. The Liverpool Telescope is operated on the island of La Palma by Liverpool John Moores University in the Spanish Observatorio del Roque de los Muchachos of the Instituto de Astrofísica de Canarias with financial support from the UK Science and Technology Facilities Council. Research at Lick Observatory is partially supported by a generous gift from Google. We thank J. Brown and M. Siebert for help with Keck observations.

The Pan-STARRS1 Surveys (PS1) have been made possible through contributions of the Institute for Astronomy, the University of Hawaii, the Pan-STARRS Project Office, the Max-Planck Society and its participating institutes, the Max Planck Institute for Astronomy, Heidelberg, and the Max Planck Institute for Extraterrestrial Physics, Garching, The Johns Hopkins University, Durham University, the University of Edinburgh, Queen's University Belfast, the Harvard-Smithsonian Center for Astrophysics, the Las Cumbres Observatory Global Telescope Network Incorporated, the National Central University of Taiwan, the Space Telescope Science Institute, the National Aeronautics and Space Administration under grant No. NNX08AR22G issued through the Planetary Science Division of the NASA Science Mission Directorate, the National Science Foundation under grant No. AST-1238877, the University of Maryland, and Eötvös Loránd University (ELTE).

This project used data obtained with the Dark Energy Camera (DECam), which was constructed by the Dark Energy Survey (DES) collaboration. Funding for the DES Projects has been provided by the U.S. Department of Energy, the U.S. National Science Foundation, the Ministry of Science and Education of Spain, the Science and Technology Facilities Council of the United Kingdom, the Higher Education Funding Council for England, the National Center for Supercomputing Applications at the University of Illinois at Urbana-Champaign, the Kavli Institute of Cosmological Physics at the University of Chicago, Center for Cosmology and Astro-Particle Physics at the Ohio State University, the Mitchell Institute for Fundamental Physics and Astronomy at Texas A&M University, Financiadora de Estudos e Projetos, Fundação Carlos Chagas Filho de Amparo, Financiadora de Estudos e Projetos, Fundação Carlos Chagas Filho de Amparo a Pesquisa do Estado do Rio de Janeiro, Conselho Nacional de Desenvolvimento Científico e Tecnológico and the Ministerio da Ciência, Tecnologia e Inovação, the Deutsche Forschungsgemeinschaft and the Collaborating Institutions in the Dark Energy Survey. The Collaborating Institutions are Argonne National Laboratory, the University of California at Santa Cruz, the University of Cambridge, Centro de Investigaciones Energéticas, Medioambientales y Tecnológicas-Madrid, the University of Chicago, University College London, the DES-Brazil Consortium, the University of Edinburgh, the Eidgenössische Technische Hochschule (ETH) Zurich, Fermi National Accelerator Laboratory, the University of Illinois at Urbana-Champaign, the Institut de Ciències de l'Espai (IEEC/CSIC), the Institut de Física d'Altes Energies, Lawrence Berkeley National Laboratory, the Ludwig-Maximilians Universität München and the associated Excellence Cluster Universe, the University of Michigan, the National Optical Astronomy Observatory, the University of Nottingham, the Ohio State University, the University of Pennsylvania, the University of Portsmouth, SLAC National Accelerator Laboratory, Stanford University, the University of Sussex, and Texas A&M University.

The national facility capability for SkyMapper has been funded through ARC LIEF grant LE130100104 from the Australian Research Council, awarded to the University of Sydney, the Australian National University, Swinburne University of Technology, the University of Queensland, the University of Western Australia, the University of Melbourne, Curtin University of Technology, Monash University and the Australian Astronomical Observatory. SkyMapper is owned and operated by The Australian National University's Research School of Astronomy and Astrophysics. The survey data were processed and provided by the SkyMapper Team at ANU. The

SkyMapper node of the All-Sky Virtual Observatory (ASVO) is hosted at the National Computational Infrastructure (NCI). Development and support the SkyMapper node of the ASVO has been funded in part by Astronomy Australia Limited (AAL) and the Australian Government through the Commonwealth's Education Investment Fund (EIF) and National Collaborative Research Infrastructure Strategy (NCRIS), particularly the National eResearch Collaboration Tools and Resources (NeCTAR) and the Australian National Data Service Projects (ANDS).


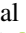

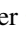




This research has made use of the SVO Filter Profile Service (<http://svo2.cab.inta-csic.es/theory/fps/>) supported from the Spanish MINECO through grant AYA2017-84089.

S.v.V. is supported by the James Arthur Postdoctoral Fellowship. S.G. is supported in part by NSF CAREER grant 1454816 and NSF AAG grant 1616566. N.R. acknowledges the support of a Joint Space-Science Institute prize postdoctoral fellowship. This project has received funding from the European Research Council (ERC) under the European Union's Horizon 2020 research and innovation program (grant agreement No. 759194—USNAC). A. Y.Q.H. is supported by a National Science Foundation Graduate Research Fellowship under grant No. DGE-1144469. This work was supported by the GROWTH project funded by the National Science Foundation under PIRE grant No. 1545949. C.F. gratefully acknowledges support of his research by the Heising-Simons Foundation (#2018-0907). The UCSC transient team is supported in part by NSF grant AST-1518052, NASA/Swift grant 80NSSC19K1386, the Gordon & Betty Moore Foundation, the Heising-Simons Foundation, and by a fellowship from the David and Lucile Packard Foundation to R.J.F.

Software: Ampel (Nordin et al. 2019), Astropy (Astropy Collaboration et al. 2018), catsHTM (Soumagnac & Ofek 2018), emcee (Foreman-Mackey et al. 2013), extcats (github.com/MatteoGiomi/extcats), gPhoton (Million et al. 2016), HEASoft (Arnaud 1996), FSPS (Conroy et al. 2009; Conroy & Gunn 2010; Foreman-Mackey et al. 2014), Prospector (Johnson & Leja 2017).

ORCID iDs

Sjoert van Velzen  <https://orcid.org/0000-0002-3859-8074>
 Suvi Gezari  <https://orcid.org/0000-0003-3703-5154>
 Erica Hammerstein  <https://orcid.org/0000-0002-5698-8703>
 Nathaniel Roth  <https://orcid.org/0000-0002-6485-2259>
 Sara Frederick  <https://orcid.org/0000-0001-9676-730X>
 S. Bradley Cenko  <https://orcid.org/0000-0003-1673-970X>
 Daniel A. Perley  <https://orcid.org/0000-0001-8472-1996>
 Jesper Sollerman  <https://orcid.org/0000-0003-1546-6615>
 Nadejda Blagorodnova  <https://orcid.org/0000-0003-0901-1606>
 Igor Andreoni  <https://orcid.org/0000-0002-8977-1498>
 Eric C. Bellm  <https://orcid.org/0000-0001-8018-5348>
 Richard Dekany  <https://orcid.org/0000-0002-5884-7867>
 Christoffer Fremling  <https://orcid.org/0000-0002-4223-103X>
 V. Zach Golkhou  <https://orcid.org/0000-0001-8205-2506>
 Matthew J. Graham  <https://orcid.org/0000-0002-3168-0139>
 Anna. Y. Q. Ho  <https://orcid.org/0000-0002-9017-3567>
 Mansi M. Kasliwal  <https://orcid.org/0000-0002-5619-4938>
 Charles D. Kilpatrick  <https://orcid.org/0000-0002-5740-7747>
 Shrinivas R. Kulkarni  <https://orcid.org/0000-0001-5390-8563>
 Thomas Kupfer  <https://orcid.org/0000-0002-6540-1484>

Russ R. Laher  <https://orcid.org/0000-0003-2451-5482>
 Ashish Mahabal  <https://orcid.org/0000-0003-2242-0244>
 Frank J. Masci  <https://orcid.org/0000-0002-8532-9395>
 Adam A. Miller  <https://orcid.org/0000-0001-9515-478X>
 Reed Riddle  <https://orcid.org/0000-0002-0387-370X>
 Ben Rusholme  <https://orcid.org/0000-0001-7648-4142>
 David L. Shupe  <https://orcid.org/0000-0003-4401-0430>
 Maayane T. Soumagnac  <https://orcid.org/0000-0001-6753-1488>

References

- Alexander, K. D., Berger, E., Guillochon, J., Zauderer, B. A., & Williams, P. K. G. 2016, *ApJ*, **819**, L25
- Alexander, K. D., Wieringa, M. H., Berger, E., Saxton, R. D., & Komossa, S. 2017, *ApJ*, **837**, 153
- Arcavi, I., Gal-Yam, A., Sullivan, M., et al. 2014, *ApJ*, **793**, 38
- Arnaud, K. A. 1996, in ASP Conf. Ser. 101, *Astronomical Data Analysis Software and Systems V*, ed. G. H. Jacoby & J. Barnes (San Francisco, CA: ASP), 17
- Astropy Collaboration, Price-Whelan, A. M., Sipőcz, B. M., et al. 2018, *AJ*, **156**, 123
- Auchettl, K., Guillochon, J., & Ramirez-Ruiz, E. 2017, *ApJ*, **838**, 149
- Bellm, E. C., Kulkarni, S. R., Barlow, T., et al. 2019a, *PASP*, **131**, 068003
- Bellm, E. C., Kulkarni, S. R., Graham, M. J., et al. 2019b, *PASP*, **131**, 018002
- Blagorodnova, N., Cenko, S. B., Kulkarni, S. R., et al. 2019, *ApJ*, **873**, 92
- Blagorodnova, N., Gezari, S., Hung, T., et al. 2017, *ApJ*, **844**, 46
- Blagorodnova, N., Neill, J. D., Walters, R., et al. 2018, *PASP*, **130**, 035003
- Blanchard, P. K., Nicholl, M., Berger, E., et al. 2017, *ApJ*, **843**, 106
- Bonnerot, C., & Lu, W. 2020, *MNRAS*, **495**, 1374
- Bonnerot, C., Rossi, E. M., & Lodato, G. 2017, *MNRAS*, **464**, 2816
- Brown, J. S., Kochanek, C. S., Holoiu, T. W.-S., et al. 2018, *MNRAS*, **473**, 1130
- Burrows, D. N., Hill, J. E., Nousek, J. A., et al. 2005, *SSRv*, **120**, 165
- Calzetti, D., Armus, L., Bohlin, R. C., et al. 2000, *ApJ*, **533**, 682
- Cannizzo, J. K., Lee, H. M., & Goodman, J. 1990, *ApJ*, **351**, 38
- Cenko, S. B., Cucchiara, A., Roth, N., et al. 2016, *ApJ*, **818**, L32
- Chambers, K. C., Magnier, E. A., Metcalfe, N., et al. 2016, arXiv:1612.05560
- Chornock, R., Berger, E., Gezari, S., et al. 2014, *ApJ*, **780**, 44
- Conroy, C., & Gunn, J. E. 2010, *ApJ*, **712**, 833
- Conroy, C., Gunn, J. E., & White, M. 2009, *ApJ*, **699**, 486
- Dai, L., McKinney, J. C., & Miller, M. C. 2015, *ApJ*, **812**, L39
- Dai, L., McKinney, J. C., Roth, N., Ramirez-Ruiz, E., & Miller, M. C. 2018, *ApJ*, **859**, L20
- Dey, A., Schlegel, D. J., Lang, D., et al. 2019, *AJ*, **157**, 168
- Dong, S., Bose, S., Chen, P., et al. 2018, *ATel*, **12198**, 1
- Dong, S., Shappee, B. J., Prieto, J. L., et al. 2016, *Sci*, **351**, 257
- Donley, J. L., Brandt, W. N., Eracleous, M., & Boller, T. 2002, *AJ*, **124**, 1308
- Evans, P. A., Beardmore, A. P., Page, K. L., et al. 2009, *MNRAS*, **397**, 1177
- Flesch, E. W. 2015, *PASA*, **32**, e010
- Foreman-Mackey, D., Hogg, D. W., Lang, D., & Goodman, J. 2013, *PASP*, **125**, 306
- Foreman-Mackey, D., Sick, J., & Johnson, B. 2014, python-fsps: Python bindings to FSPS (v0.1.1), Zenodo, doi:10.5281/zenodo.12157
- Fremling, C., Sollerman, J., Taddia, F., et al. 2016, *A&A*, **593**, A68
- Fremling, U. C., Miller, A. A., Sharma, Y., et al. 2020, *ApJ*, **895**, 32
- French, K. D., Arcavi, I., & Zabludoff, A. 2016, *ApJ*, **818**, L21
- French, K. D., Arcavi, I., & Zabludoff, A. 2017, *ApJ*, **835**, 176
- Gaia Collaboration, Brown, A. G. A., Vallenari, A., et al. 2018, *A&A*, **616**, A1
- Gaia Collaboration, Prusti, T., de Bruijne, J. H. J., et al. 2016, *A&A*, **595**, A1
- Gehrels, N., Chincarini, G., Giommi, P., et al. 2004, *ApJ*, **611**, 1005
- Gezari, S., Basa, S., Martin, D. C., et al. 2008, *ApJ*, **676**, 944
- Gezari, S., Chornock, R., Rest, A., et al. 2012, *Natur*, **485**, 217
- Gezari, S., Heckman, T., Cenko, S. B., et al. 2009, *ApJ*, **698**, 1367
- Gezari, S., Hung, T., Cenko, S. B., et al. 2017, *ApJ*, **835**, 144
- Gezari, S., Martin, D. C., Milliard, B., et al. 2006, *ApJ*, **653**, L25
- Gezari, S., van Velzen, S., Cenko, S. B., et al. 2018, *ATel*, **12035**, 1
- Gezari, S., van Velzen, S., Perley, D. A., et al. 2019, *ATel*, **12789**, 1
- Graham, M. J., Kulkarni, S. R., Bellm, E. C., et al. 2019, *PASP*, **131**, 078001
- Graur, O., French, K. D., Zahid, H. J., et al. 2018, *ApJ*, **853**, 39
- Guillochon, J., Manukian, H., & Ramirez-Ruiz, E. 2014, *ApJ*, **783**, 23
- Guillochon, J., & Ramirez-Ruiz, E. 2013, *ApJ*, **767**, 25
- Heikkilä, T., Reynolds, T., Kankare, E., et al. 2019, *ATel*, **12529**, 1
- Hills, J. G. 1975, *Natur*, **254**, 295

- HI4PI Collaboration, Ben Bekhti, N., Flöer, L., et al. 2016, *A&A*, **594**, A116
- Holoien, T. W. S., Auchettl, K., Tucker, M. A., et al. 2020, *ApJ*, **898**, 161
- Holoien, T. W.-S., Brown, J. S., Auchettl, K., et al. 2018, *MNRAS*, **480**, 5689
- Holoien, T. W.-S., Huber, M. E., Shappee, B. J., et al. 2019b, *ApJ*, **880**, 120
- Holoien, T. W.-S., Kochanek, C. S., Prieto, J. L., et al. 2016a, *MNRAS*, **463**, 3813
- Holoien, T. W.-S., Kochanek, C. S., Prieto, J. L., et al. 2016b, *MNRAS*, **455**, 2918
- Holoien, T. W.-S., Prieto, J. L., Bersier, D., et al. 2014, *MNRAS*, **445**, 3263
- Holoien, T. W. S., Vallety, P. J., Auchettl, K., et al. 2019a, *ApJ*, **883**, 111
- Hung, T., Cenko, S. B., Roth, N., et al. 2019, *ApJ*, **879**, 119
- Hung, T., Gezari, S., Blagorodnova, N., et al. 2017, *ApJ*, **842**, 29
- Jiang, N., Dou, L., Wang, T., et al. 2016, *ApJL*, **828**, L14
- Johnson, B., & Leja, J. 2017, bd-j/prospector: Initial Release, v.v0.1, Zenodo, doi:10.5281/zenodo.1116491
- Jonker, P. G., Stone, N. C., Genozov, A., van Velzen, S., & Metzger, B. 2020, *ApJ*, **889**, 166
- Kara, E., Dai, L., Reynolds, C. S., & Kallman, T. 2017, *MNRAS*, **474**, 3593
- Kasliwal, M. M., Cannella, C., Bagdasaryan, A., et al. 2019, *PASP*, **131**, 038003
- Kippenhahn, R., & Weigert, A. 1990, *Stellar Structure and Evolution* (Berlin: Springer)
- Kochanek, C. S. 2016, *MNRAS*, **461**, 371
- Komossa, S. 2015, *JHEAp*, **7**, 148
- Krolik, J., Piran, T., Svirski, G., & Cheng, R. M. 2016, *ApJ*, **827**, 127
- LaMassa, S. M., Cales, S., Moran, E. C., et al. 2015, *ApJ*, **800**, 144
- Law-Smith, J., Ramirez-Ruiz, E., Ellison, S. L., & Foley, R. J. 2017, *ApJ*, **850**, 22
- Leloudas, G., Dai, L., Arcavi, I., et al. 2019, *ApJ*, **887**, 218
- Lidskii, V. V., & Ozernoi, L. M. 1979, *SvAL*, **5**, 16
- Liu, X.-L., Dou, L.-M., Shen, R.-F., & Chen, J.-H. 2019, arXiv:1912.06081
- Lodato, G., King, A. R., & Pringle, J. E. 2009, *MNRAS*, **392**, 332
- Lodato, G., & Rossi, E. M. 2011, *MNRAS*, **410**, 359
- Lu, W., & Kumar, P. 2018, *ApJ*, **865**, 128
- Mahabal, A., Rebbapragada, U., Walters, R., et al. 2019, *PASP*, **131**, 038002
- Mainzer, A., Bauer, J., Grav, T., et al. 2011, *ApJ*, **731**, 53
- Martin, D. C., Fanson, J., Schiminovich, D., et al. 2005, *ApJL*, **619**, L1
- Masci, F. J., Laher, R. R., Rusholme, B., et al. 2019, *PASP*, **131**, 018003
- Mendel, J. T., Simard, L., Palmer, M., Ellison, S. L., & Patton, D. R. 2014, *ApJS*, **210**, 3
- Metzger, B. D., & Stone, N. C. 2016, *MNRAS*, **461**, 948
- Metzger, B. D., & Stone, N. C. 2017, *ApJ*, **844**, 75
- Miller, J. M., Kaastra, J. S., Miller, M. C., et al. 2015, *Natur*, **526**, 542
- Miller, M. C. 2015, *ApJ*, **805**, 83
- Million, C., Fleming, S. W., Shiao, B., et al. 2016, *ApJ*, **833**, 292
- Mockler, B., Guillochon, J., & Ramirez-Ruiz, E. 2019, *ApJ*, **872**, 151
- Mummery, A., & Balbus, S. A. 2020, *MNRAS*, **492**, 5655
- Nicholl, M., Blanchard, P. K., Berger, E., et al. 2019a, *MNRAS*, **488**, 1878
- Nicholl, M., Short, P., Angus, C., et al. 2019b, *ATel*, **12752**, 1
- Nicholl, M., Short, P., Lawrence, A., Ross, N., & Smartt, S. 2019c, *TNSAN*, **59**, 1
- Nicholl, M., Wevers, T., Oates, S. R., et al. 2020, arXiv:2006.02454
- Nordin, J., Brinnel, V., van Santen, J., et al. 2019, *A&A*, **631**, A147
- Oke, J. B. 1974, *ApJS*, **27**, 21
- Pasham, D. R., Cenko, S. B., Sadowski, A., et al. 2017, *ApJL*, **837**, L30
- Pasham, D. R., & van Velzen, S. 2018, *ApJ*, **856**, 14
- Patterson, M. T., Bellm, E. C., Rusholme, B., et al. 2019, *PASP*, **131**, 018001
- Piran, T., Svirski, G., Krolik, J., Cheng, R. M., & Shiokawa, H. 2015, *ApJ*, **806**, 164
- Rees, M. J. 1988, *Natur*, **333**, 523
- Rigault, M., Neill, J. D., Blagorodnova, N., et al. 2019, *A&A*, **627**, A115
- Roming, P. W. A., Kennedy, T. E., Mason, K. O., et al. 2005, *SSRv*, **120**, 95
- Roth, N., Kasen, D., Guillochon, J., & Ramirez-Ruiz, E. 2016, *ApJ*, **827**, 3
- Schawinski, K., Urry, C. M., Simmons, B. D., et al. 2014, *MNRAS*, **440**, 889
- Shiokawa, H., Krolik, J. H., Cheng, R. M., Piran, T., & Noble, S. C. 2015, *ApJ*, **804**, 85
- Siebert, M. R., Strasburger, E., Rojas-Bravo, C., & Foley, R. J. 2019, *ATel*, **13131**, 1
- Soumagnac, M. T., & Ofek, E. O. 2018, *PASP*, **130**, 075002
- Steele, I. A., Smith, R. J., Rees, P. C., et al. 2004, *Proc. SPIE*, **5489**, 679
- Stern, D., Assef, R. J., Benford, D. J., et al. 2012, *ApJ*, **753**, 30
- Stoughton, C., Lupton, R. H., Bernardi, M., et al. 2002, *AJ*, **123**, 485
- Strauss, M. A., Weinberg, D. H., Lupton, R. H., et al. 2002, *AJ*, **124**, 1810
- Strubbe, L. E., & Quataert, E. 2009, *MNRAS*, **400**, 2070
- Tachibana, Y., & Miller, A. A. 2018, *PASP*, **130**, 128001
- Tucker, M. A., Huber, M., Shappee, B. J., et al. 2018, *ATel*, **11444**, 1
- van Velzen, S. 2018, *ApJ*, **852**, 72
- van Velzen, S., Farrar, G. R., Gezari, S., et al. 2011, *ApJ*, **741**, 73
- van Velzen, S., Gezari, S., Cenko, S. B., et al. 2018, *ATel*, **12263**, 1
- van Velzen, S., Gezari, S., Cenko, S. B., et al. 2019e, *ApJ*, **872**, 198
- van Velzen, S., Gezari, S., Frederick, S., et al. 2019d, *ATel*, **12509**, 1
- van Velzen, S., Gezari, S., Hung, T., et al. 2019a, *ATel*, **12568**, 1
- van Velzen, S., Gezari, S., Ward, C., et al. 2019b, *TNSAN*, **88**, 1
- van Velzen, S., Holoien, T. W. S., Onori, F., Hung, T., & Arcavi, I. 2020, *SSRv*, **216**, 124
- van Velzen, S., Mendez, A. J., Krolik, J. H., & Gorjian, V. 2016, *ApJ*, **829**, 19
- van Velzen, S., Stone, N. C., Metzger, B. D., et al. 2019c, *ApJ*, **878**, 82
- Wevers, T., Pasham, D. R., van Velzen, S., et al. 2019a, *MNRAS*, **488**, 4816
- Wevers, T., Stone, N. C., van Velzen, S., et al. 2019b, *MNRAS*, **487**, 4136
- Wevers, T., van Velzen, S., Jonker, P. G., et al. 2017, *MNRAS*, **471**, 1694
- Wolf, C., Onken, C. A., Luvaul, L. C., et al. 2018, *PASA*, **35**, e010
- Wryzykowski, Ł., Zieliński, M., Kostrzewa-Rutkowska, Z., et al. 2017, *MNRAS*, **465**, L114